Geochemistry, Geophysics, Geosystems®

AGU ADVANCING EARTH AND SPACE SCIENCES

RESEARCH ARTICLE
10.1029/2023GC011381

Testing Mantle Convection Simulations With Paleobiology and Other Stratigraphic Observations: Examples From Western North America

Victoria M. Fernandes[1,2], **Gareth G. Roberts**[2], **and Fred Richards**[2]

[1]GFZ Potsdam, Helmholtz Zentrum, Potsdam, Germany, [2]Department of Earth Science and Engineering, Imperial College London, London, UK

Key Points:

- Large-scale digital inventories of stratigraphic observations used to test predictions from mantle convection simulations
- Useful diagnostics include net uplift and subsidence, absolute elevations, paleo-water depths
- Upper mantle thermo-mechanical evolution—crucial for assessing sub-plate support—constrained using stratigraphy

Supporting Information:

Supporting Information may be found in the online version of this article.

Correspondence to:

V. M. Fernandes and G. G. Roberts,
milanez@gfz-potsdam.de;
gareth.roberts@imperial.ac.uk

Citation:

Fernandes, V. M., Roberts, G. G., & Richards, F. (2024). Testing mantle convection simulations with paleobiology and other stratigraphic observations: Examples from Western North America. *Geochemistry, Geophysics, Geosystems*, *25*, e2023GC011381. https://doi.org/10.1029/2023GC011381

Received 29 NOV 2023
Accepted 8 MAY 2024

Author Contributions:

Conceptualization: Victoria M. Fernandes, Gareth G. Roberts
Formal analysis: Victoria M. Fernandes
Funding acquisition: Gareth G. Roberts
Investigation: Victoria M. Fernandes, Fred Richards
Methodology: Victoria M. Fernandes
Project administration: Gareth G. Roberts
Resources: Fred Richards
Software: Victoria M. Fernandes
Supervision: Gareth G. Roberts
Validation: Victoria M. Fernandes

Abstract Mantle convection plays a fundamental role in driving evolution of oceanic and continental lithosphere. In turn it impacts a broad suite of processes operating at or close to Earth's surface including landscape evolution, glacio-eustasy, magmatism, and climate. A variety of theoretical approaches now exist to simulate mantle convection. Outputs from such simulations are being used to parameterize models of landscape evolution and basin formation. However, the substantial body of existing simulations has generated a variety of conflicting views on the history of dynamic topography, its evolution and key parameters for modeling mantle flow. The focus of this study is on developing strategies to use large-scale quantitative stratigraphic observations to assess model predictions and identify simulation parameters that generate realistic predictions of Earth surface evolution. Spot measurements of uplift or subsidence provide useful target observations for models of dynamic topography, but finding areas where tectonics have not also influenced vertical motions is challenging. To address this issue, we use large inventories of stratigraphic data from across North America with contextual geophysical and geodetic data to constrain the regional uplift and subsidence history. We demonstrate that a suite of typical geodynamic simulations struggle to match the amplitude, polarity and timing of observed vertical motions. Building on recent seismological advances, we then explore strategies for understanding patterns of continental uplift and subsidence that incorporate (and test) predicted evolution of the lithosphere, asthenosphere and deep mantle. Our results demonstrate the importance of contributions from the uppermost mantle in driving vertical motions of continental interiors.

1. Introduction

1.1. Overview

Mantle convection is generally accepted as an important driver of horizontal and vertical lithospheric motions (i.e., uplift and subsidence; Gurnis et al., 2000; Hager & Richards, 1989; Hoggard et al., 2021; D. McKenzie & Jarvis, 1980; Parsons & Daly, 1983; Pekeris, 1935). In turn, lithospheric motion in response to mantle convection appears to play a key role in driving diverse geological, geomorphological, glacio-eustatic and climatic processes (e.g., Austermann et al., 2015; F. D. Richards et al., 2023; Salles et al., 2017; Stephenson et al., 2019). As such, there is considerable interest in developing reliable means to determine the history of mantle convection and its role in dictating the history of Earth's surface. An important challenge is to produce or identify data of sufficient quality and spatio-temporal density to either directly constrain histories of mantle convection, or test the fidelity of geodynamic simulations. In this contribution, we explore the use of substantial, digital, inventories of stratigraphic and paleobiological data to test vertical motion histories predicted by models of mantle convection. In our view, stratigraphic observations are the least equivocal constraints on histories of lithospheric vertical motion available and provide a crucial test of geodynamic simulations.

It is generally accepted that mantle convection is expressed in geological and geomorphological processes including the generation of topography (e.g., Hager et al., 1985; Parsons & Daly, 1983; M. A. Richards & Hager, 1984), creation of accommodation space in sedimentary basins (e.g., Lodhia et al., 2018; Morris et al., 2020), changes in sea level (e.g., Moucha, Forte, Rowley, et al., 2008; Moucha, Forte, Mitrovica, et al., 2008), flooding of continental interiors and shoreline deformation and generation of stratigraphic hiatuses (e.g., Hayek et al., 2020; Rovere et al., 2015; Rowley et al., 2013; Vilacís et al., 2022). It also appears to determine the planform and relief of continental drainage patterns (e.g., Cox, 1989; Czarnota et al., 2014; Faccenna et al., 2019; Lipp & Roberts, 2021; G. G. Roberts, Paul, et al., 2012; G. G. Roberts, White, et al., 2012). In turn it

Visualization: Victoria M. Fernandes
Writing – original draft: Victoria M. Fernandes
Writing – review & editing: Gareth G. Roberts, Fred Richards

likely impacts many related phenomena operating at, or close to, Earth's surface, including climate (Conway-Jones & White, 2022). Constraining amplitudes and histories of dynamic topography across scales of interest is clearly crucial for understanding Earth's surface evolution. For mantle convection, these scales include wavelengths, λ, set by the elastic strength of plates ($O(10-10^2)$ km), to global scales (spherical harmonic degree, $l=2$, $\lambda=O(10^4)$ km; Ghelichkhan et al., 2021; Holdt et al., 2022; Müller et al., 2018). Methodologies to constrain sub-plate support sit in two broad categories.

First, geological, geophysical and geomorphological observations have been used to constrain modern and historic dynamic topography at specific localities (e.g., Ball et al., 2021; Fernandes et al., 2019; Holdt et al., 2022; Morris et al., 2020). The clearest observational guide to amplitudes, wavelengths and spectral power of modern dynamic topography arise from fitting spherical harmonic functions to oceanic age-depth measurements (e.g., Hoggard et al., 2020; Holdt et al., 2022; Valentine & Davies, 2020, strictly, models are fit to residuals from calibrated oceanic plate cooling histories).

The second suite of methodologies use geodynamic simulators to predict dynamic topography across the scales of interest (e.g., Bunge & Baumgardner, 1995; Colli et al., 2016; Flament et al., 2013; Ghelichkhan et al., 2021; Gurnis, 1988; Hager & Richards, 1989; D. P. McKenzie et al., 1974; Müller et al., 2018). This approach, which now often makes use of geological (e.g., plate motion histories) and geophysical (e.g., seismic tomography) observations and theory to prescribe model properties (e.g., conversion of acoustic velocities into density; assimilation of tomographic models), provides means to explore theoretical responses and sensitivities of dynamic topography to calculated mantle evolution (e.g., Davies et al., 2023; Faccenna et al., 2019; Flament et al., 2013; Forte et al., 2009; L. Liu et al., 2008; Müller et al., 2018). There now exists a considerable body of mantle convection simulations, a few of which have been compared to independent geological observations at specific localities (e.g., New Jersey Margin, North America; Flament et al., 2013) and to global power spectra of ocean age-depth residuals (Hoggard et al., 2016). Model predictions, such as uplift and subsidence, have recently been coupled with models of lithospheric and landscape evolution to predict development of drainage networks and sedimentary basins (e.g., Ding et al., 2023; Faccenna et al., 2019; Salles et al., 2017; Wang et al., 2020).

Assessing sub-plate support of continents is generally more challenging than for oceans. The variability and complexity of continental lithosphere rheology, structure, and density complicate efforts to disentangle dynamic and isostatic contributions to topography (see, e.g., Hoggard et al., 2021; Stephenson et al., 2021). Nonetheless, assessing predictions, and changes, of continental sub-plate support has recently become considerably more tractable due to the improved availability of stratigraphic data (e.g., Macrostrat, Paleobiology Database). These data can be combined with geophysical observations (e.g., seismology; gravity anomalies) as well as other geological (e.g., magmatic) and geomorphological observations to constrain geometries and histories of sub-plate support (e.g., Fernandes & Roberts, 2021a, 2021b). As an example, in this paper we focus on Western North America, where stratigraphic data is dense and well documented. Additionally, a large body of magmatic and geophysical data is available to test predictions of mantle convection simulations. A considerable body of information regarding contextual tectonic histories (e.g., crustal shortening, extension and plate flexure) also exists, which is crucial for extricating signals of sub-plate support from geological observations (e.g., DeCelles, 1994).

Available stratigraphic observations include paleo-water depth information recorded in the Paleobiology Database (PBDB), developed by the paleobiological community, and stratigraphic data that record transitions from marine to terrestrial deposition (e.g., Hintze & Kowallis, 2009). These data have the important benefit of requiring few corrections, bar minor, relatively well constrained adjustments for compaction and denudation (see, e.g., Fernandes & Roberts, 2021a, 2021b). There are of course many other indirect constraints on lithospheric vertical motions including thermochronometry, palynology, isotope altimetry, histories of sedimentary flux, stratigraphic hiatuses, and landform geometries, which can be used to fill in spatio-temporal stratigraphic gaps (e.g., Blum & Pecha, 2014; Chamberlain et al., 2012; Fernandes et al., 2019; Flowers & Farley, 2012; Flowers et al., 2008, 2012; Galloway et al., 2011; Hayek et al., 2020; Huntington et al., 2010; G. G. Roberts, Paul, et al., 2012; G. G. Roberts, White, et al., 2012; Vilacís et al., 2022). However, we think it is important to make a distinction between information provided from such approaches and the more direct constraints on elevation, uplift and subsidence that arise from interrogating the stratigraphic archive. One of the main advantages of using this approach is that it can provide information about the magnitude and history of net vertical motions, without recourse to proxies or independent information (e.g., lapse rates, geotherms, interpolation, erosional models). It is of course limited to constraining net vertical motion and by the loci of preserved stratigraphy.

In the following sections, first, existing geological constraints on the history of vertical motions of the North American Western Interior are summarized. Second, predictions of dynamic topography from mantle circulation models are compared to geological observations. We identify model parameterizations that best match geological observations. Similar to a variety of other geodynamic studies, the dynamic topography predictions we make use of were generated without including the shallowest few hundred kilometers of the mantle (e.g., Flament et al., 2013; Müller et al., 2018; Young et al., 2022). Thus, third, geophysical observations of the upper mantle are combined with isostatic models to explore asthenospheric and lithospheric contributions to uplift in the region. The isostatic models we develop make use of seismological and stratigraphic observations to explore contributions to North American topography from asthenospheric thermal anomalies and modification of lithospheric depletion and structure. Finally, we quantify uncertainties and sensitivities via Monte Carlo error propagation, and discuss the implications of our findings for assessing predictions of dynamic topography from geodynamic models.

1.2. Global Observations of Sub-Plate Support

Potential field and seismological observations combined with magmatism, geomorphology and stratigraphy have been used to quantify modern sub-plate support and histories of dynamic topography (e.g., Ball et al., 2021; Gurnis, 1990; Gurnis et al., 2000; Klöcking et al., 2018; G. G. Roberts, Paul, et al., 2012; G. G. Roberts, White, et al., 2012; Stephenson et al., 2019). The relative simplicity and consistency of oceanic lithospheric structure and rheologies, combined with increasingly tightly constrained thermal histories, make it well suited for identifying signals of sub-plate support. For example, the age and isostatically corrected basement depths of oceanic basins have been used to measure residuals from ocean plate cooling models with amplitudes up to O(1) km (e.g., Crough, 1983; Hoggard et al., 2016; Menard, 1969; Panasyuk & Hager, 2000; F. Richards, Hoggard, Crosby, et al., 2020; F. D. Richards, Hoggard, White, & Ghelichkhan, 2020; Valentine & Davies, 2020). A recent, extensive, compilation of measurements across all oceanic basins indicates that residual surface deflections are measurable to wavelengths at least as low as ∼900 km (spherical harmonic degree 40; Holdt et al., 2022). These near global-scale compilations of residual topography paint a detailed picture of the present-day state of dynamic topography along continental margins and within oceanic basins. The power spectra of oceanic residual depths indicate that both deep mantle flow and shallower processes, likely involving interaction between the asthenosphere and lithosphere, are fundamental for generating Earth's dynamic surface response. Deep mantle flow primarily contributes to dynamic topography at long wavelengths ($\sim 10^4$ km), and shallower processes control shorter wavelength contributions (10^2–10^3 km; Colli et al., 2016; Parsons & Daly, 1983; F. Richards, Hoggard, Crosby, et al., 2020; F. D. Richards, Hoggard, White, & Ghelichkhan, 2020). As an example, consider Atlantic oceanic lithosphere abutting eastern North America, which has residuals of up to ±1 km (Holdt et al., 2022). Backstripping of stratigraphy preserved along this passive margin indicates that sub-plate drawdown generated 500–900 m of water-loaded subsidence during the last ∼20 Ma (Morris et al., 2020).

Global compilations of melt fractions of young (Neogene-Quaternary) mafic rocks and upper mantle shear wave velocity anomalies have recently been shown to be broadly negatively correlated (Ball et al., 2021). For example, mafic samples in western North America are concentrated atop slow upper mantle shear-wave velocity anomalies. Many continental regions underlain by relatively slow upper mantle shear wave velocity anomalies, including Western North America, are also associated with uplifted marine rock (Fernandes et al., 2019). Such stratigraphy, preserved atop continental interiors and on fringing sedimentary basins, provides opportunities to constrain histories of sub-plate support (Fernandes & Roberts, 2021a, 2021b). Elevated Quaternary marine terraces and warped shorelines provide the least equivocal constraints on vertical lithospheric motions, but are limited to the more recent geological past (e.g., Austermann et al., 2017). Older paleo-water depth indicators preserved in the marine rock record can be used to extend these constraints further into the geological past (e.g., Bessin et al., 2017; Dickinson et al., 1988). A general challenge is generating observations at sufficient scale and density to directly constrain histories of sub-plate support at $O(10^2 - 10^3)$ km wavelengths. Building on the methodologies developed by Ziegler et al. (1985), Sahagian (1988), and Rowley et al. (2013), Fernandes and Roberts (2021a, 2021b) generated an inventory of 24,372 measurements of Late Cretaceous to Recent net uplift. These measurements were generated by combining records of Cretaceous to Recent marine rock documented in the Paleobiology Database (PBDB) with estimates of elevation, paleobathymetry, compaction, and global sea level change. The distribution of recorded marine rock is of course not uniform across all continents. Nonetheless,

most continents have stratigraphic observations preserved in sedimentary basins and atop uplifted topography that are suited to testing predictions of geodynamic models.

1.3. Geodynamic Modeling

A variety of methodologies exist to retrodict mantle convection. A widely used approach inverts mantle structure derived from seismological (tomographic) models of Earth's interior, and can incorporate Supporting Information S1 (e.g., plate motion histories). Methods for prescribing temperature, density and viscosity fields, and also surface velocities, that drive mantle convection simulations vary (see e.g., Flament et al., 2013; Forte, 2000; Forte et al., 2007, 2009, 2010; Ghelichkhan et al., 2021; Gurnis, 1990; Hager et al., 1985; Müller et al., 2018; Spasojević & Gurnis, 2012). As such, associated models have differing predictive capabilities. Some constrain the present-day state of the mantle and its rate of change, whilst those generated using backwards advection, adjoint or data assimilation methods make predictions of how dynamic topography has changed in the geological past (see, e.g., Ghelichkhan et al., 2021). We note that a significant number of mantle convection simulations do not include the shallowest 200–350 km of the mantle in part because of the computational challenges associated with accurately modeling large changes in viscosity between the lithosphere and asthenosphere, uncertain lithospheric structure and rheologies, and difficulty of accurately incorporating boundary layer dynamics on numerical simulations. This approach makes it challenging to ascertain the role the dynamic shallow mantle plays in generating topography. Given that simulations of mantle convection are often extremely computationally expensive, we think it is prudent to develop strategies to identify existing simulations that are consistent with available observations.

Here, we focus on testing predictions generated by Müller et al. (2018) because they examined a diverse range of parameterizations, and made their predictions available for testing. We use their outputs in a plate reference frame. Some of their models incorporate backwards advection, suppress the formation of plumes, and do not incorporate the shallowest few hundred kilometers into predictions of dynamic topography. As they discuss in their paper, such approaches may reduce the realism of predicted dynamic topography, especially at shorter wavelengths. A focus of this study is on examining whether contributions from the uppermost convecting mantle and lithosphere, which might include isostatic effects associated with heating asthenosphere and changes in lithospheric mantle thickness or density, are crucial for generating observed vertical lithospheric motions (e.g., Colli et al., 2016). First, we explain why Western North America was chosen to test model predictions.

2. North American Dynamic Topography: Observations and Theory

2.1. Geophysical and Stratigraphic Framework

A considerable body of geophysical and geological data across North America constrains the present-day state of its crust, lithospheric and sub-lithospheric mantle, and therefore isostatic contributions to topography, with higher fidelity than most places on Earth. These include, but are not limited to USArray-derived seismic velocities of the crust and mantle, active source seismology, gravity anomalies and associated estimates of elastic thickness and dynamic support, and stratigraphic observations (see, e.g., Buehler & Shearer, 2016; Crough, 1983; Fernandes & Roberts, 2021a, 2021b; Hoggard et al., 2021; Laske et al., 2013). Additionally, isotopic paleoaltimetry, thermochronometry, sedimentary flux histories, mafic melting histories, and geomorphic observations and theory provide contextual information about the evolution of North American topography and sub-plate support (see, e.g., Fernandes et al., 2019, for summary). Inverse modeling of longitudinal river profiles provides one way to fill spatio-temporal gaps between spot measurements (e.g., Fernandes et al., 2019; G. G. Roberts, Paul, et al., 2012; G. G. Roberts, White, et al., 2012). Nonetheless, disentangling tectonic (e.g., shortening, extension) and sub-lithospheric contributions to elevations is especially fraught along the western continental margin where tectonic processes and terrane accretion have dominated its recent geological history. Instead, we focus on Cretaceous to Recent stratigraphy in the North American Western Interior (Figure 1).

In our view, the least equivocal, most direct, constraints on histories of North American vertical lithospheric motion arise from the distribution of ancient marine rock (e.g., Ziegler et al., 1985). Biostratigraphic information contained within these rocks (e.g., age, paleo-water depth) provide crucial clues about the elevation of Earth's surface at specific times, typically when it is at, or close to, contemporaneous sea level. By combining these data with their compaction and denudation histories, spot measurements of post-deposition uplift can be generated for substantial tracts of North American topography (Fernandes & Roberts, 2021a, 2021b). The present-day elevation

10.1029/2023GC011381

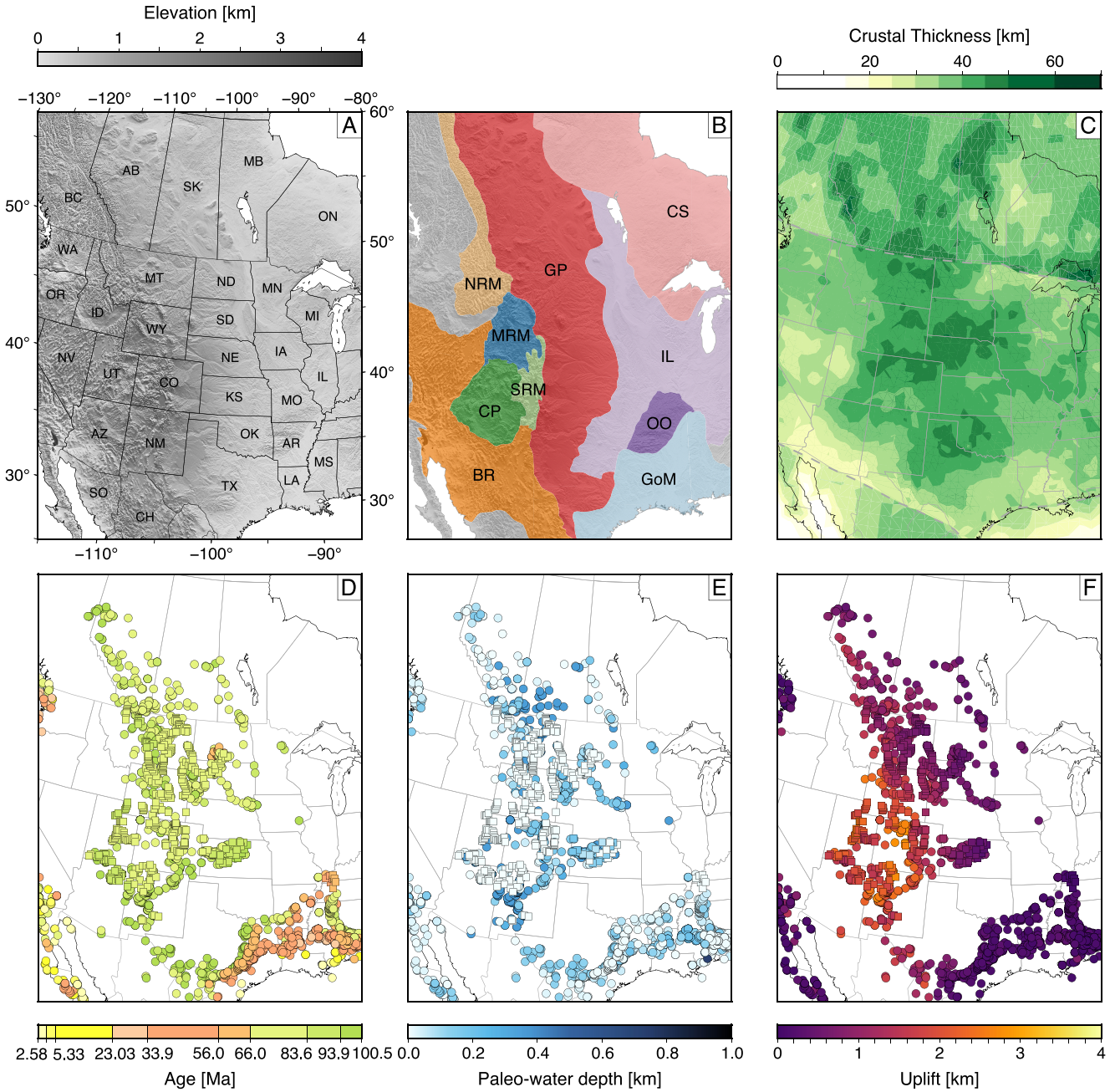

Figure 1. Western North America and its surroundings. (a) Hill-shaded elevation map showing USA, Canadian and Mexican state borders, note two-letter state abbreviations (SRTM+; Becker et al., 2009). (b) Physiographic provinces after Fenneman (1928): CS = Canadian Shield; GP = Great Plains; NRM, MRM, SRM = Northern, Middle and Southern Rocky Mountains; CP = Colorado Plateau; BR = Basin and Range; IL = Interior Lowlands; OO = Ozark and Ouachita Mountains; GoM = Gulf of Mexico Coastal Plain. (c) Crustal thickness from CRUST1 (Laske et al., 2013) and PnUS (Buehler & Shearer, 2016). Dashed gray lines = extent of PnUS model. (d) Location of fossil assemblages from the Paleobiology Database (PBDB; circles) indicating youngest outcropping marine to terrestrial (MTT; squares) stratigraphic transitions (Fernandes & Roberts, 2021a, 2021b; Fernandes et al., 2019). Points are colored by stratigraphic age, using the Gradstein et al. (2012) timescale (see Figure S1 in Supporting Information S1 for colorblind-friendly version). (e) Interpreted paleo-water depth for each location. (f) Net uplift calculated from fossil and stratigraphic data.

of marine fossil assemblages recorded in the PBDB, for example, provide constraints on post-Cretaceous net uplift in the Great Plains (GP), Rocky-Mountains-Colorado-plateau, Basin and Range (BR), and Interior Lowlands (IL) (Figure 1). In addition, stratigraphic sections throughout North America record facies transitions from marine to non-marine depositional environments, which can be used to calculate precise rates of net uplift (e.g.,

Hampson, 2010; Hintze & Kowallis, 2009). Building on the body of stratigraphic observations generated by Crough (1983), Ziegler et al. (1985) and others, Fernandes et al. (2019) compiled 339 locations where such stratigraphic transitions are observed in outcropping stratigraphy of the North American Western Interior. Stratigraphy from these locations typically feature as part of well-established chronostratigraphic frameworks that include radiometric dating (Cobban et al., 2006; Lynds & Slattery, 2017; Merewether & McKinney, 2015; Merewether et al., 2011; Obradovich & Cobban, 1975). Thicknesses and distributions of Cretaceous rocks from outcrop and well data (e.g., Mancos Shale) are of special importance because of their role in defining when marine conditions likely last prevailed across large tracts of the continental interior (Bond, 1976; Cross & Piliger, 1978; Li & Aschoff, 2022; L. N. R. Roberts & Kirschbaum, 1995).

The subsidence history of the region is also well documented from well and outcrop data. Tectonic processes (lithospheric shortening, extension, plate flexure) evidently generated Cretaceous to Recent accommodation space and uplifted sedimentary rock (e.g., in the BR province, Rio Grange Rift, Sevier-Laramide piggy-back basins and forelands; Cross, 1986; Cross & Piliger, 1978; Dickinson, 2004; Dickinson et al., 1988). For example, during Cretaceous flooding >12 km of sediment was deposited in small, isolated, probably flexural basins (e.g., L. N. R. Roberts & Kirschbaum, 1995). Nonetheless, the distribution of uplifted marine rock and subsidence patterns indicate that such tectonic processes cannot explain $O(1)$ km subsidence at horizontal scales >1,000 km. Instead, mantle convective drawdown likely played an important role in generating accommodation space at these scales (e.g., Mitrovica et al., 1989; Pang & Nummedal, 1995). In this paper we explore how such observations of net vertical lithospheric motion can be used to assess predictions from geodynamic models.

2.2. Quantifying Net Vertical Motions From Stratigraphy

2.2.1. Uplift

We quantify uplift using the data compilations of marine fossil assemblages with a known paleo-water depth, and stratigraphic markers of the youngest outcropping transition between marine and non-marine depositional environments presented in Fernandes et al. (2019) and Fernandes and Roberts (2021a, 2021b). Together, these constraints comprise >2,000 spot measurements of net uplift. Regressive stratigraphic sequences were identified from published facies interpretations (e.g., Gani et al., 2015; Johnson et al., 2002; L. N. R. Roberts & Kirschbaum, 1995), and ages were tied using published regional chronostratigraphy (Figure 1d; Cobban et al., 2006; Lynds & Slattery, 2017; Merewether & McKinney, 2015; Merewether et al., 2011; Obradovich & Cobban, 1975). Particular care was taken to identify lateral and temporal variability in the depositional facies sequences. Depositional environments, interpreted using fossil assemblages, were converted to paleo-water depth using the paleo-bathymetric model described by Fernandes and Roberts (2021a, 2021b, Figure 1e). Elevations and paleo-sea level ranges were extracted from ETOPO1 and the compilation of Bessin et al. (2017), respectively.

A demonstration of the methodology for estimating net surface uplift, U, from fossil assemblages is shown in Figure 2. This figure shows uplift of a fossil assemblage from the Book Cliffs Utah corrected for paleo-water depth, eustatic sea level and compaction. Uplift is calculated simply by incorporating measured modern elevations of fossil assemblages, E, paleobathymetry, B, sea level at the time of deposition, S, a correction for post-depositional compaction, ΔC, and their associated uncertainties (δE, δB, δS, $\delta \Delta C$). Such that $U = E + B - S + \Delta C$ and $\delta U = \left[(\delta E)^2 + (\delta B)^2 + (\delta S)^2 + (\delta \Delta C)^2\right]^{1/2}$. Global eustasy and paleo-water depths are usually the largest sources of uncertainty, nonetheless they rarely exceed a few hundred meters for the assemblages used in this study (see Fernandes & Roberts, 2021a, 2021b, for extended methodology and the inventory of uplift constraints and calculated uncertainties). Net dynamic topography extracted from Model M2 of Müller et al. (2018) is also shown in Figure 2 to illustrate our approach to extracting commensurate (in time) predictions.

The spatial and temporal distribution of paleo-biological data provide constraints on the magnitude of net uplift experienced at each location, and paleo-elevation of the surface at the time of deposition. This information constrains both the absolute paleo-elevation of the region, as well as the magnitude and polarity of net post-deposition vertical motion. Using such inventories of geological observations means that suites of spot measurements can be used to identify vertical motions associated with changes in elevation at the scales predicted by mantle convection models (e.g., >1,000 km; i.e., larger than deflections determined by flexural rigidity of the

10.1029/2023GC011381

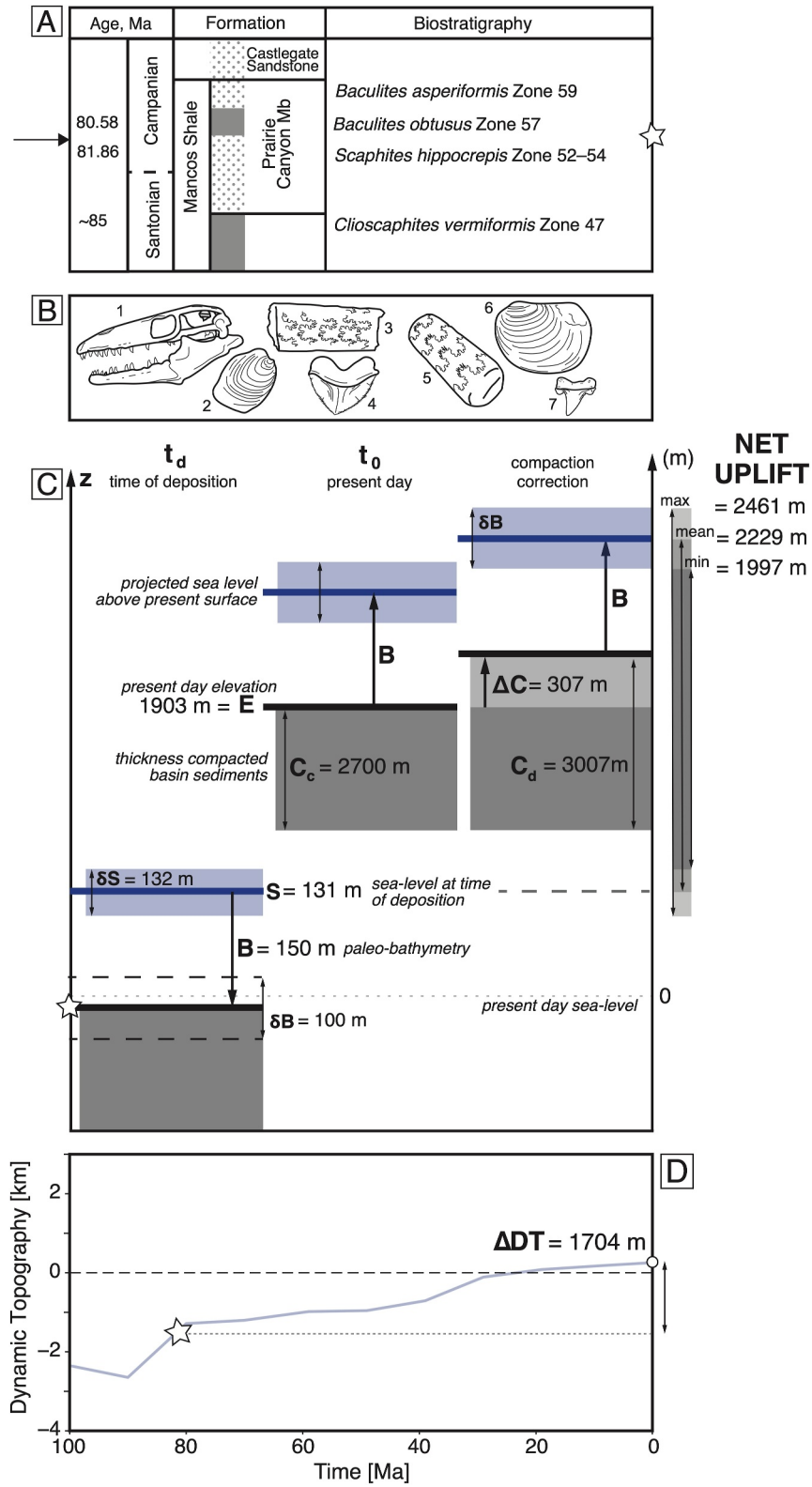

Figure 2.

lithosphere). The fossil and stratigraphic data set we make use of covers 3,500 × 2,350 km, with a sample density of ∼1 sample per km^2 in the densest regions (Figure 1d).

There are a variety of means to assess long wavelength contributions to measured uplift (e.g., fitting spherical harmonic functions to spot measurements; Hoggard et al., 2016). Given that we focus on a single continental region, a simple way to do so is to fit splines to spot measurements. We seek gridded surfaces that require the least smoothing of data and allow the amplitude of measurements to be preserved (Figure 1). The resultant grid was filtered using a 1,000-km low-pass Gaussian filter and is shown in Figure 3a. A histogram showing the difference between the grid and spot measurements of uplift is shown in Figure 3b. Most spot measurements record a dominantly large-scale, >1,000 km, uplift signal, shown by a difference of less than ±200 m for >65% of the spot measurements. Small-scale deviations from the large-scale pattern of uplift are generally associated with tectonic structures generated principally during Laramide deformation and basin-forming tectonic events (see, e.g., Dickinson et al., 1988; DeCelles, 2004). Grids generated using alternative low-pass cut-offs are shown in Figure S2 in Supporting Information S1.

2.2.2. Subsidence

Additional constraints on the vertical motions of Western North America were provided by the subsidence history of the Western Interior Basin. Basin stratigraphy recorded in individual wells has been flexurally backstripped to reveal a spatially and temporally variable subsidence pattern (see Figures S4–S6 in Supporting Information S1; S. Liu et al., 2014). However, individual wells do not constrain the history of subsidence on a sufficiently large scale to accurately reflect the broader geodynamic history of the basin. In order to expand this data set to larger spatial scales, following Mitrovica et al. (1989), we calculate subsidence by backstripping existing regional isopach maps. First, isopach maps from L. N. R. Roberts and Kirschbaum (1995) were digitized using QGIS software. The published isopach figures for each time slice were geo-referenced, and contour lines were individually traced to create a vector map of the contour lines where the thickness value of each line is an attribute. Next, using GRASS functionalities, the vector map was rasterized by creating a 10 × 10 min grid, where each grid cell is either a contour line cell (containing the sediment thickness value), or a fill cell. Using the r.surf.cont functionality, a linear interpolation between contour intervals was performed using a flood fill algorithm. Gridding by fitting a regularized spline with tension was also tested, however this methodology produced unwanted data artifacts in regions where the contour lines were too closely spaced. The best-fit isopach maps are shown in Figure S4 in Supporting Information S1.

Air-loaded subsidence histories were calculated by backstripping the isopach maps. Admittance between gravity and topography, and their associated coherence, indicates that the elastic thickness of the lithosphere, T_e, beneath the North American Western Interior is <40 km and as low as ∼10 km atop the Colorado Plateau (CP) (Audet, 2014; Stephenson et al., 2014). These results suggest that it is reasonable to assume isostasy prevails when backstripping. The isopach maps were decompacted using the compaction parameterization of Athy (1930). We assumed a compaction wavelength $\lambda = 2$ km and initial porosity $\phi_\circ = 0.6$, typical for sandstones (Sclater & Christie, 1980). Minimum and maximum subsidence was calculated by assuming 0 and 3 km thickness of post-Cretaceous sediment was preserved atop Cretaceous rock, respectively. Maximum thickness of post-Cretaceous rocks were estimated from average thicknesses preserved in boreholes and outcrops in the area (e.g., Hintze & Kowallis, 2009). In order to compare the subsidence histories with dynamic topography predictions, decompacted subsidence was isostatically air-loaded assuming a density of sedimentary rock, $\rho_s = 2{,}400$ kg m^{-3}. The resultant grids of calculated subsidence are shown in Figure S5 in Supporting Information S1 and are summarized for specific localities of interest in Figure 6. These maps are in broad agreement with previous studies, providing a large-scale spatio-temporal history of subsidence (see Cross & Piliger, 1978; Mitrovica et al., 1989). The pattern

Figure 2. Illustration of methodologies used to extract observed and predicted net uplift from geological data and predictions from mantle convection simulations. Loci of the fossil assemblage in the Book Cliffs of Utah and dynamic topographic prediction is labeled '3' in Figure 3. (a) General stratigraphic framework of the Mancos Shale, and associated bio- and chrono-stratigraphic constraints. (b) Fossil assemblage used to constrain the paleo-bathymetry of the Prairie Canyon Member of the Mancos Shale: 1—Prognathodon, 2—Platyceramus cycloides, 3—Baculites haresi, 4—Squalicorax pristodontus, 5—Baculites aquilaensis, 6—Innoceramus balticus, 7—Cretolamna (see Fernandes & Roberts, 2021a, 2021b, for more details). (c) Schematic showing net uplift calculation and corrections; see Section 2.2.1 for description of symbols and methodology; C_c and C_d = compacted and decompacted stratigraphy. (d) History of dynamic topography from Model M2 of Müller et al. (2018) at the location of the fossil assemblage. The star marks the age of deposition of the fossil assemblage. Net predicted dynamic topography, ΔDT, is calculated as the difference between predicted dynamic topography at the time of deposition and the present-day.

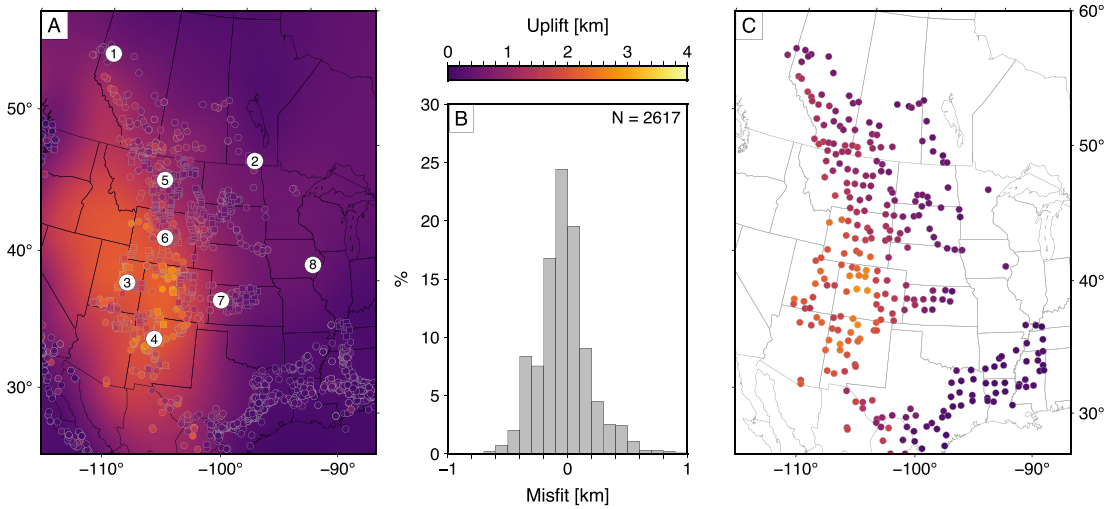

Figure 3. Large-scale patterns of uplift. (a) Smooth surface fit to 2,617 spot measurements of uplift derived from the PBDB (circles) and marine to terrestrial stratigraphic transitions (squares). Large numbered circles = localities where stratigraphic observations of vertical motion and predicted dynamic topography are shown in Figure 4D and Supporting Information S1. Surface was generated using continuous curvature splines and then filtered to remove wavelengths <1,000 km. (b) Difference between uplift estimated from 2,617 stratigraphic (PBDB) observations and the smooth surface shown in panel a. (c) Location and mean uplift value for uplift data averaged into 1° × 1° bins ($N = 295$). Data from the westernmost edge of the North American continent were not included as their uplift history most likely does not reflect a history of mantle-driven vertical motions.

and magnitude of subsidence predicted from this simple method was compared to subsidence estimates for the same time intervals generated from backstripping of data from individual wells (colored circles in Figure 6; S. Liu et al., 2014). There is generally a good agreement between the well data and the subsidence grids, both in the spatial distribution and the magnitude of subsidence.

The results suggest that parts of the westernmost portion of the study region, that is, the BR and CP, experienced subsidence due to lithospheric thinning and loading. Backstripping of well data predict a higher magnitude of subsidence in the Late Campanian, which is likely due to a combination of grid smoothing and choice of compaction parameterization. We now have a body of uplift and subsidence data from across Western North America with which we can test predictions from geodynamic simulations of mantle convection.

3. Testing Histories of Dynamic Topography From Mantle Convection Simulations

3.1. Introduction

A substantial body of published mantle convection simulations predict dynamic topography of Western North America (see, e.g., Davies et al., 2023; Flament et al., 2013; Forte et al., 2007, 2009; L. Liu et al., 2008; S. Liu et al., 2014; Moucha, Forte, Rowley, et al., 2008; Moucha, Forte, Mitrovica, et al., 2008; Müller et al., 2018; Rovere et al., 2015). We focus on testing predictions of dynamic topography from the seven models presented by Müller et al. (2018). Their paper describes their methodologies in depth and clearly explains challenges and potential pitfalls in comparing model predictions to independent geologic observations. An important issue they discuss, which we address below, is exclusion of the upper few hundred kilometers of the Earth from calculations of dynamic topography. In short, they test different parameterizations including variations in viscosity, thermal expansivity, density, activation energies and initial conditions. They also test models that contain plumes and models in which plume formation is suppressed. The models can be placed into three categories based on their parameterizations, each of which make broadly similar predictions: M1, M2–M4, and M5–M7. In model M1 mantle flow is computed by a backwards integration of the temperature field wherein the direction of gravity and plate motions are reversed (L. Liu et al., 2008; Spasojević & Gurnis, 2012). The other models are driven by forward thermal convection with plate velocities applied as surface boundary conditions using a modified version of CitcomS (Müller et al., 2018). The main difference between the M2–M4 and M5–M7 families of models lies within their viscosity structures; M5–M7 models have mantle viscosities that are lower by $O(10 - 10^2)$, and a much larger viscosity contrast between the lithosphere and asthenosphere (asthenosphere viscosity being 500× lower, when compared to 10× lower in models M2–M4). For all models, average model resolution is

$50 \times 50 \times 15$ km at Earth's surface. Predicted dynamic topography and its incremental change for each model is shown in Supporting Information S1.

Examples of predicted net change in dynamic topography from each category are shown in Figures 4a–4c. Grids of calculated net dynamic topography were generated by subtracting values from a specific time in the past (e.g., 90, 80, 70, or 60 Ma) from present-day values (see, e.g., Figure 4a). By doing so we can compare changes in predicted dynamic topography to net uplift or subsidence recorded by stratigraphy. Each group of models generated significantly different predictions of the history, spatial distribution and amplitude of dynamic topography. We compare absolute elevations and net vertical motions recorded by stratigraphy to predictions of net dynamic topography.

3.2. General Insights From Testing Geodynamic Predictions Using Geologic Observations

Müller et al. (2018) compared their dynamic topographic predictions to power spectra of ocean-age depth residuals and to paleo-geographic maps generated by, for example, Smith et al. (1994) and Heine et al. (2015). Most of the models over-predict power calculated from ocean-age depth residuals at spherical harmonic degrees 1–2 (wavelengths $\approx 2.2 \pm 0.6 \times 10^4$ km; see their Figure 5), despite having excised the top 300 km of the upper mantle, which contain strong long-wavelength anomalies. Models M5–M7 most closely match spectra of residual depth anomalies at degrees 2–3 ($\lambda \approx 1.4 \pm 0.3 \times 10^4$ km), but under-predict power at higher degrees. Models M1–M4 more closely match at degrees 3–5 ($\lambda \approx 0.9 \pm 0.2 \times 10^4$ km). In other words, none of the models match the entire power spectrum of ocean age-depth residual at degrees 1–5, but some provide a reasonably good fit at specific scales. Paleo-geographic maps were also used to identify regions submerging or emerging with respect to sea level at given time periods. These data were used to constrain the polarity of vertical lithospheric motions (i.e., uplift or subsidence). Their preferred model, which most closely matches continental inundation by seaways, is the forward geodynamic simulation M7, which suppresses plumes. We explore whether amplitudes and net change in vertical lithospheric motion provide additional useful information to discriminate between models. In this study, we test the model predictions using geological observations in three ways.

First, amplitude and polarity of net dynamic topographic change since the Late Cretaceous are compared to spot measurements from the PBDB augmented by 339 spot measurements that tightly constrain the timing of transition from marine to terrestrial conditions. We select eight specific localities with different tectonic and lithospheric settings across the continent to demonstrate our approach (Figures 1 and 10, Figure S3 in Supporting Information S1). The seven geodynamic models predict net uplift for most of the North American Western Interior since the late Cretaceous, however the pattern and amplitude of uplift significantly vary between models. As an example of the diversity of model predictions, consider Figures 4d–4g, which shows calculated dynamic topography in Alberta, Manitoba, Utah and New Mexico (see Figure 4a). Predicted net dynamic topography was extracted at the same location and for the same duration as each PBDB and stratigraphic constraint (see, e.g., Figure 2).

Second, predictions of the absolute amplitude of dynamic topography in the Late Cretaceous are compared to paleo-water depth estimates from the PBDB and additional stratigraphic constraints. Air-loaded predictions of dynamic topography from the geodynamic models (D_{air}) were isostatically corrected to a water-load (D_w)

$$D_{air} = D_w \frac{\rho_a}{\rho_a - \rho_w} \approx 1.43 D_w. \quad (1)$$

where ρ_a and ρ_w is the density of asthenospheric mantle and water, respectively. To extract predicted water-loaded dynamic topography at a specific time (e.g., the time of deposition of the fossil assemblage in Figure 2, 81.22 Ma) the discrete time steps (e.g., 80, 90 Ma) of Müller et al. (2018) were linearly interpolated (see blue line in Figure 2d). Thus, predicted dynamic topography at the location and time of deposition of each fossil assemblage was extracted and compared to the observed paleo-bathymetry (interpreted from the fossil record).

Finally, the history of Late Cretaceous dynamic topographic vertical motions are compared to the subsidence history of the Western Interior Basin. Figure 6 shows the Late Cretaceous vertical motions at four key locations (shown in Figure 4a). For each location, the first panel shows paleo-water depth of fossil assemblages located within a 50 km radius of dynamic topography predicted by the geodynamic models. The second panel shows the predicted net change in dynamic topography for each Late Cretaceous stage: Cenomanian, Turonian, Santonian-Coniacian, lower Campanian, upper Campanian, and Maastrichtian. The final panel shows the range of isopach

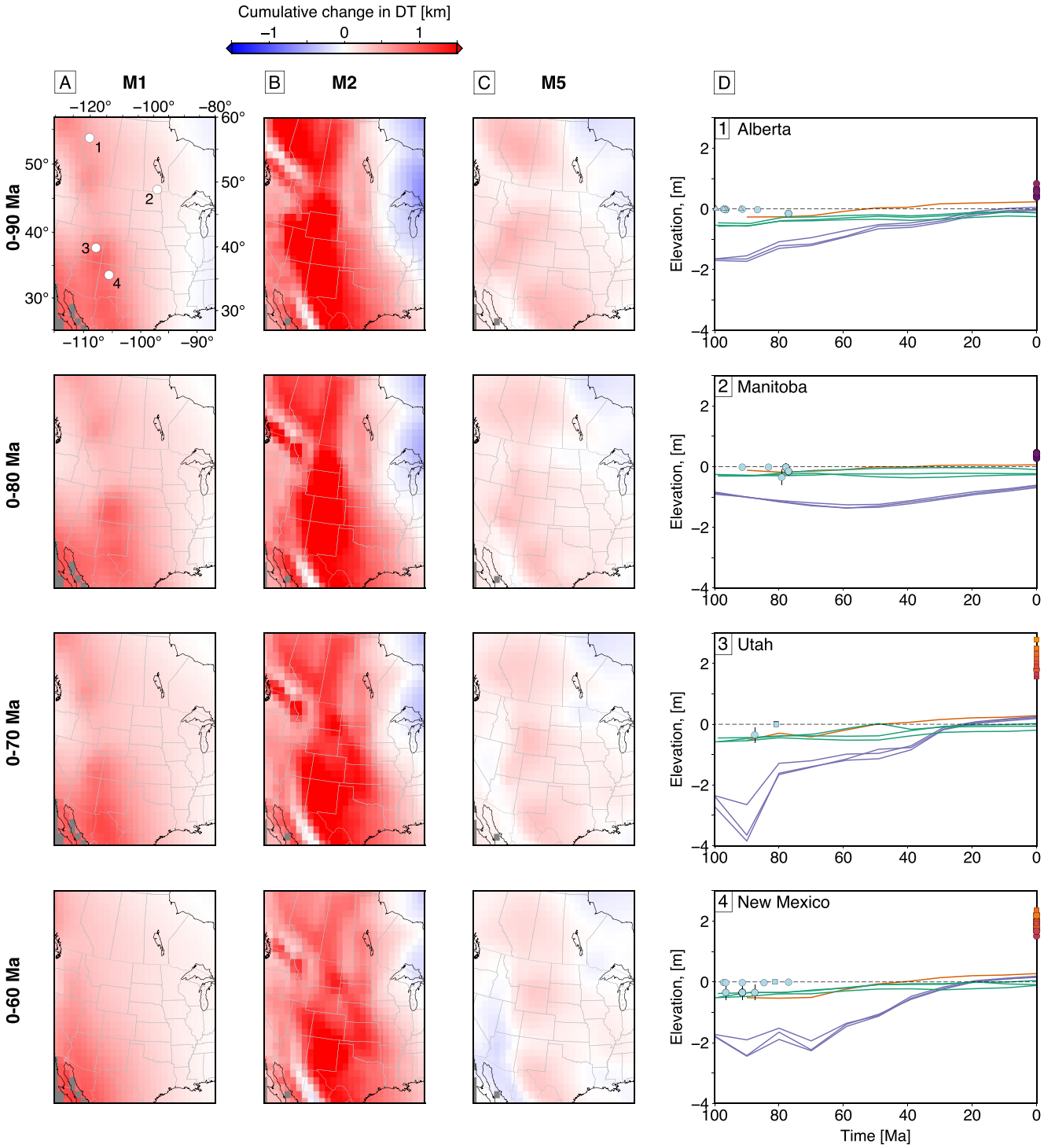

Figure 4. Comparison of dynamic topography predicted from mantle convection simulations and stratigraphic observations. Maps show cumulative change in dynamic topography since 90, 80, 70, and 60 Ma predicted by models (a) M1, (b) M2, and (c) M5, which are representative histories produced by families of models generated by Müller et al. (2018). Gray lines = state/country boundaries (see Figure 1a). Labeled white circles = locations of stratigraphic constraints and predicted dynamic topography shown in panel (d): Alberta (1), Manitoba (2), Utah (3), New Mexico (4). (d) Histories of vertical motion predicted by geodynamic models compared to stratigraphic observations at localities labeled 1–4 in panel (a). Orange, purple, green lines = predicted dynamic topography from models M1, M2–M4, M5–M7, respectively (Müller et al., 2018). Circles and squares = stratigraphic observations from PBDB and first recorded terrestrial sediments, respectively, and modern topography; error bars = paleo-water depth uncertainties (colors indicate paleo-water depth, see Figure 1e; see body text for details).

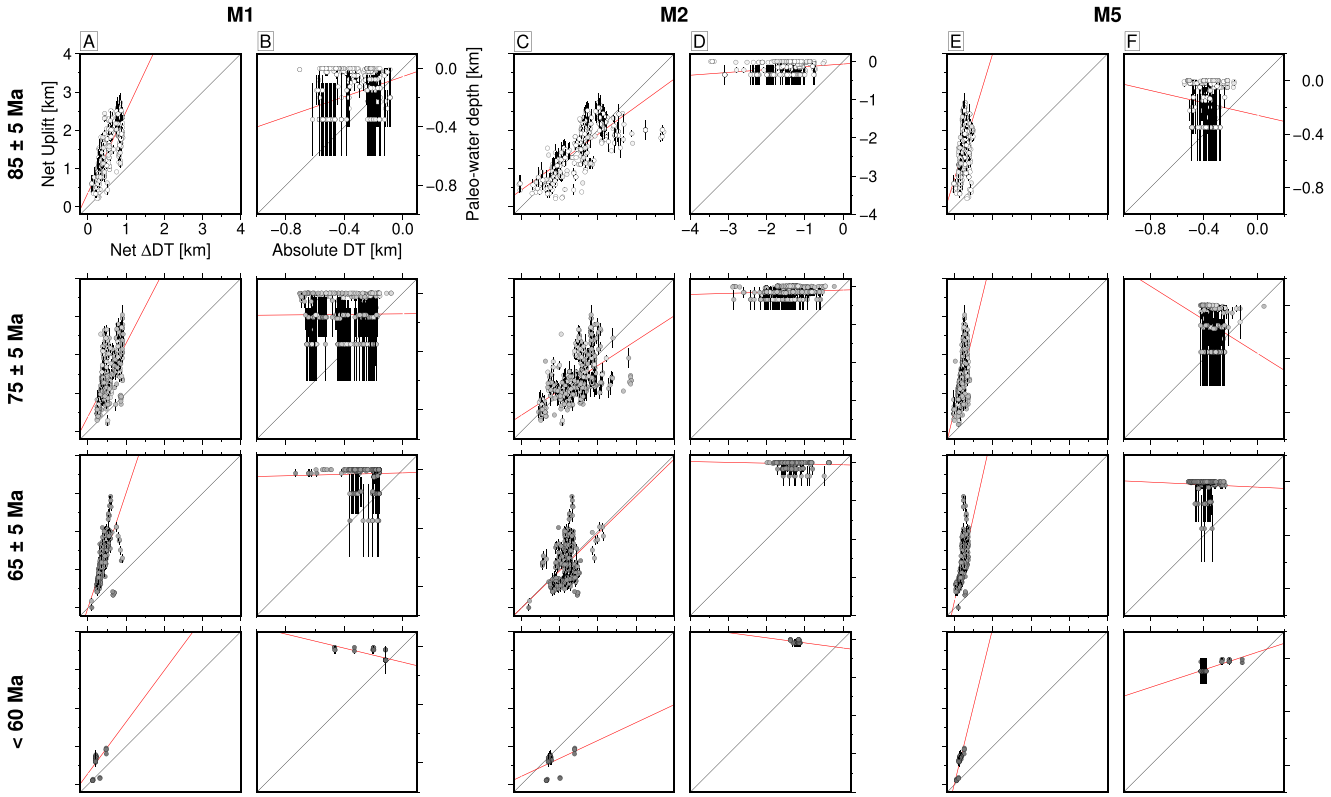

Figure 5. Comparisons of net (post-deposition) uplift and paleo-water depths from stratigraphic observations to geodynamic model predictions. (a) Circles = net uplift measured using modern elevation of marine rock compared to net change in predicted dynamic topography (see e.g. Figure 2). Measurements of net uplift are grouped according to age of deposition in 85 ± 5 Ma (top row), 75 ± 5 Ma, 65 ± 5 Ma, and <60 Ma (bottom row) bins (see Figures 1f and 2). Predictions of net dynamic topography (ΔDT) are from model M1 of Müller et al. (2018). Measured and predicted motions were averaged in the same 1° × 1° bins prior to insertion into this panel (see Figure 2); error bars = 1 standard deviation from the mean vertical stratigraphic motions within each 1 × 1° bin, which includes age and paleo-water depth uncertainties and the range of values in each bin. Black line = 1:1 relationship; red line = best-fit linear least-squares regression. (b) Comparison of predicted absolute elevations from model M1 and paleo-water depth estimates from stratigraphy in labeled age bins. (c, d) Model M2. (e, f) Model M5. See Figure 3.

thicknesses within a 50 km radius of the point, isostatic subsidence from backstripping the isopach maps of L. N. R. Roberts and Kirschbaum (1995), and a subsidence curve from S. Liu et al. (2014). In all cases, the continuous subsidence of the Western Interior Basin in the Late Cretaceous requires that the net vertical motion of the surface is negative. However, with the exception of point 8, located in the eastern-most edge of the Western Interior Basin, all models predict dynamic uplift of the North American Western Interior in the Late Cretaceous.

In the following subsections we summarize the specific parameterizations, described in detail by Müller et al. (2018), and predictions from each group of models. The fidelity of predicted dynamic topography is then assessed by comparison to the inventory of stratigraphic data.

3.3. Geodynamic Model M1

Model M1 uses the plate reconstruction of Gurnis et al. (2012), and is equivalent to the hybrid model of Spasojević and Gurnis (2012, their model *M2*). The global mantle temperature field at present-day is estimated using tomographic inversions of different seismic phases (surface and body waves using the S20RTS model in the lower mantle, and Benioff zone seismicity for the upper mantle). The temperature field is back-integrated using the backward integration method of L. Liu and Gurnis (2008). A hybrid paleo-buoyancy field is generated by merging the calculated backward-advected mantle temperature field with synthetic subducted slabs assimilated into the model based on location of subduction zones (Spasojević & Gurnis, 2012). The model has a Rayleigh number, $Ra = 7.5 \times 10^7$. Air-loaded dynamic topography is calculated with a no-slip surface boundary condition, with the top 250 km of mantle removed from the calculation. The power spectra of dynamic topography predictions show that model M1 has the highest power at spherical harmonic degree $l = 1 - 3$ for all examples

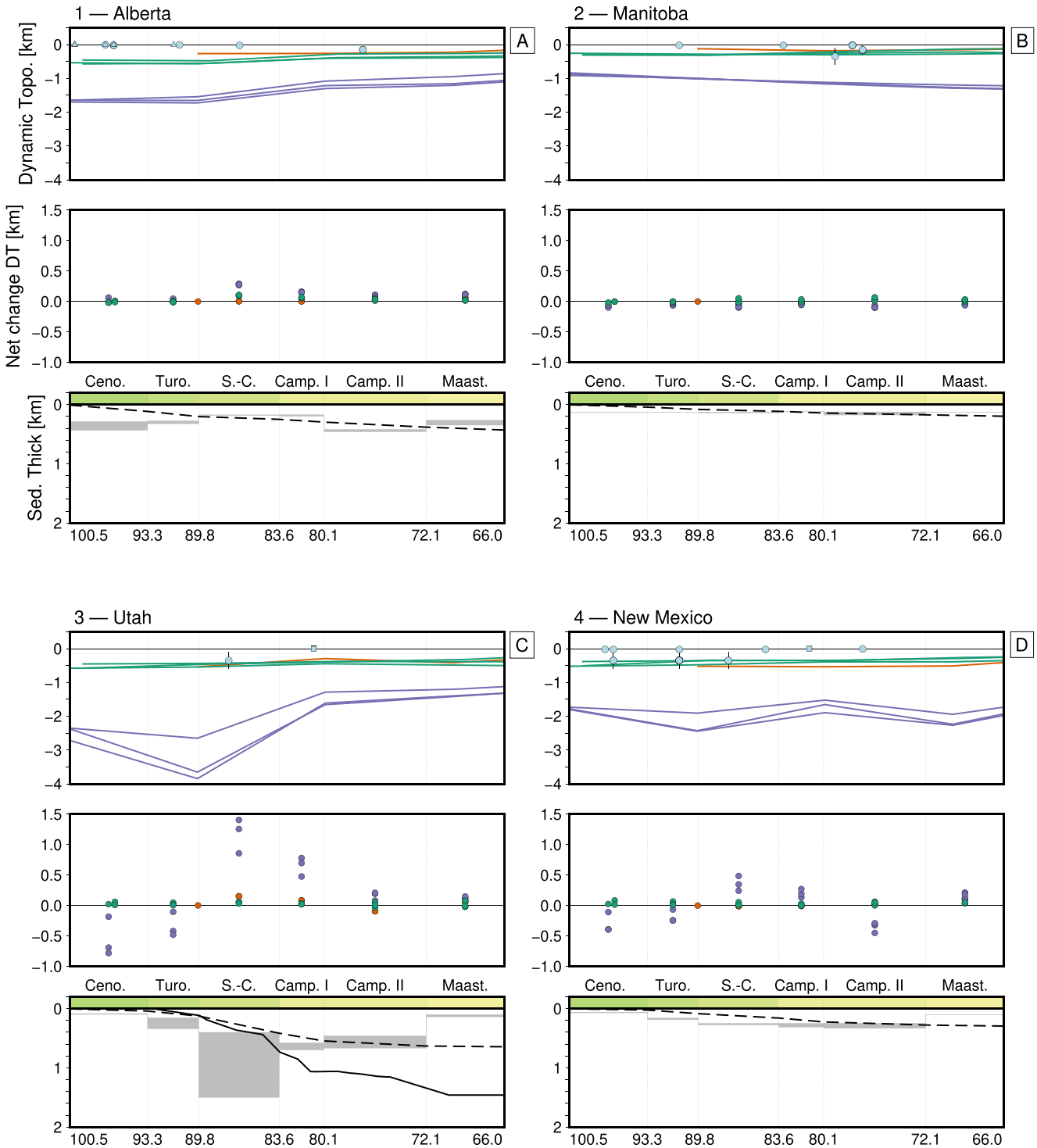

Figure 6. Comparison of predicted Late Cretaceous dynamic topography and independent subsidence histories. (a) Observations and predictions from bin (width = 30 km) centered on circle labeled 1 in Figure 2 (Alberta). Top panel: Orange, purple, green lines = predicted dynamic topography from models M1, M2–M4, M5–M7, respectively (Müller et al., 2018). Circles = paleo-water depths from biostratigraphic observations; error bars = associated uncertainties, note that in many cases uncertainty is less than symbol size. Triangles = minimum paleo-water depth from marine biostratigraphic constraints where paleo-environment is poorly constrained. Squares = first recorded post-marine terrestrial sediments (Fernandes et al., 2019). Vertical lines bound geological stages. Middle panel: Net change in predicted dynamic topography during each stage for the seven mantle convective simulations (colors as for lines in panel a); Ceno = Cenomanian, Turo = Turonian, S-C = Coniacian-Santonian, Camp I and Camp II = Campanian, Maast = Maastrichtian. Negative/positive values indicate predicted net subsidence/uplift. Bottom panel: Black dashed line = subsidence history from backstripping, decompacting, and air-loading isopach maps from L. N. R. Roberts and Kirschbaum (1995), see Supporting Information S1. Gray bands = sediment thickness within bin for each stage, also from L. N. R. Roberts and Kirschbaum (1995). (b) Manitoba (centered on circle labeled 2 in Figure 2a). (c) Utah (3). (d) New Mexico (4). Black solid line is air-loaded subsidence curve from Well 3 (−110.178°, 39.435°) presented in Liu et al. (2014).

considered by Müller et al. (2018). It predicts highest amplitudes of dynamic topography at wavelengths >10, 000 km. Comparisons between observed and predicted net vertical motions since 85 ± 5, 75 ± 5, 65 ± 5, and <60 Ma are shown in Figure 5a. For each scatter plot, a linear regression was fit using a least-squares residual misfit calculation. Model M1 tends to under-predict net uplift of Cretaceous to earliest Cenozoic marine rocks. Observed and predicted paleo-water depths for model M1 are shown in Figures 5e–5h, along with a least-squares regression fit through the data. The range of predicted Cretaceous to Cenozoic water-loaded elevations is somewhat larger than those constrained by biostratigraphic data. However, we note that many of the points coincide with the 1:1 line within error.

3.4. Models M2-M4

Models M2–M4 are characterized by initial conditions that include a 113 km thick basal thermochemical layer above the core-mantle boundary (CMB) that is 4.2% denser than ambient mantle, which acts to suppresses plume formation. This dense basal layer has the same thickness as the lower thermal boundary layer. They explore the consequences of assuming constant thermal expansion and temperature-dependent viscosity. The models have a $Ra = 7.8 \times 10^7$. Model M2 uses the plate reconstruction of Seton et al. (2012), and is equivalent to Model 3 from Müller, Flament, et al. (2016). Model M3 uses the plate reconstruction of Müller, Flament, et al. (2016) and is equivalent to Model 2 described in Müller, Flament, et al. (2016). Model M4 uses the relative plate motions of Müller, Flament, et al. (2016), absolute plate velocities of Van der Meer et al. (2010), and is equivalent to model (case) 24 from Flament et al. (2017).

For models M2–M4 (and M5–M7), dynamic topography is calculated from surface vertical stress resulting from mantle flow in restarts of the model in which the surface boundary condition is free-slip and top 350 km is removed from the calculations. Lateral viscosity variations are preserved in the rest of the mantle. The power spectra of predicted dynamic topography from all models show that for models M1–M4 the highest power resides at spherical harmonic degree $l = 2$.

The amplitude of observed net uplift is best matched by models M2, M3, and M4 (see Figure 5c). These models predict a large amplitude drawdown at ∼90 Ma, ranging from −1.5 to −4 km, and subsequent net uplift to ∼0 km at present day. Uplift is highest in the West (Arizona, Colorado, Wyoming) with a smooth decrease to the East (Illinois, Wisconsin). If all of the uplift was dynamic in origin, these results would suggest that the present-day topography of the North American Western Interior may not be dynamically supported, but instead owes its history of vertical motions to recovery from Cretaceous drawdown caused by subduction of the Farallon slab (Spasojević & Gurnis, 2012). As such, any additional sources of vertical motions would be negligible. Models M2–M4 predict as much as 1.5 km of uplift near the CP (near the Utah-Colorado border) during Santonian-Coniacian times (83.6–89.8 Ma). Conversely, the stratigraphic record indicates water-loaded subsidence of ∼100–500 m and up to 1.5 km of sediment accumulation during this time. As far as we are aware, there is no evidence for a widespread stratigraphic unconformity that might be expected to have been generated as a consequence of 1.5 km of regional uplift during this time.

M2–M4 predict up to ∼1 km of water-loaded Cretaceous subsidence, with a sharp uplift pulse (with magnitude up to 1.5 km) between 90 and 70 Ma that is not observed in the paleo-water depth record. In general the amplitude of elevations predicted from the geodynamic models (up to −4 km) overestimate observed, mostly neritic, O(10) m, paleo-water depths.

3.5. Models M5–M7

Models M5–M7 are based on examples presented in Hassan et al. (2015) and Barnett-Moore et al. (2017). Plumes are present in models M5–M6 due to a 100 km thick, 2.5% denser basal thermochemical layer above the CMB that is thinner than the basal thermal boundary layer (300 km). Like models M2–M4, M7 contains a 113 km basal thermochemical layer above the CMB made of 10% denser than ambient mantle, which suppresses plume formation. All models assume a mantle adiabat, where thermal expansion is set to decrease with depth (i.e., background mantle temperature is depth-dependent). They have an initial potential temperature of 1,252°C and a temperature drop of 952°C between thermal boundary layers. Viscosity variation with temperature is parameterized using Arrhenius laws. The models incorporate viscous dissipation and adiabatic heating, internal radiogenic heating, and have a $Ra = 5 \times 10^8$. Model M5 is equivalent to model *M3* developed by Hassan et al. (2015) and incorporates the plate reconstruction of Seton et al. (2012), with modifications for the Arctic from Shephard

et al. (2013), and modified absolute plate motions from Shephard et al. (2014). Model M6 uses plate reconstructions of Müller, Flament, et al. (2016) and Müller, Seton, et al. (2016) and is equivalent to model *C1* of Barnett-Moore et al. (2017).

Models M5–M7 have highest power at degree $l = 1$. Power drops off by more than an order of magnitude between $l = 3$ and 5. Models M5–M7 significantly under-predict the amplitude of net uplift. Nor can these models fully explain the large-scale surface tilt of the North American Western Interior. Conversely, the absolute amplitudes of models M5–M7 tend to match observed paleo-water depth within error. An important consideration is that sediment infill of accommodation space generated by dynamic drawdown could result in the maintenance of shallow paleo-water depths. This hypothesis can be investigated using the history of basement subsidence and sediment accumulation in the Western Interior Basin (e.g., Figure 6).

3.6. Summary of Predicted Dynamic Support, Observations, and Next Steps

The predictions of dynamic topography from models M1–M7 are successful at recreating the broad patterns of uplift and drawdown of the North American Western Interior. Similarly, they have been shown to agree with broad patterns of continental inundation estimated using the fossil record (Müller et al., 2018). However, some substantial discrepancies between the geological record of large-scale vertical motions and predictions from geodynamic models exist. For instance, predicted dynamic topography is inconsistent with amplitudes and polarities of net post-Cretaceous vertical motions in the North American Western Interior (Figures 4–6). Similarly, predicted paleo-bathymetries of the Western Interior Basin also tend to be discrepant (Figure 4). It is intriguing that models that predict paleo-bathymetry with some fidelity tend to be poor predictors of net changes in vertical motions, and vice versa (e.g., Figure 5). As Müller et al. (2018) discuss, an obvious source of discrepancy between observations and model predictions is excising contributions from the lithosphere and uppermost convecting mantle (uppermost 250–350 km) from predictions of vertical motions, which is common practice in such studies (see, e.g., Section 3.1).

Increasingly comprehensive seismological, magmatic and potential field observations are beginning to generate coherent views on the thickness and density of North American lithosphere, which simplifies isolation of subplate support (e.g., Ball et al., 2021; Buehler & Shearer, 2016; Hoggard et al., 2021). Thus, in the rest of this paper, we seek to establish whether relatively simple isostatic calculations and geophysical observations of the uppermost convecting mantle and lithosphere beneath North America can be used to reconcile discrepancies between predictions from Models M1–M7 (that incorporate deeper structure) and the observations. We then finish this paper by briefly discussing alternative approaches to predict dynamic support and how they might be tested using the observations.

4. Assessing Shallow Mantle Contributions to Modern Topography

It is well known that uplift and subsidence at, or close to, Earth's surface are often dominated by the thermal and structural evolution of the lithosphere (e.g., Watts, 2001). Changes in asthenospheric buoyancy via thermal expansion also appear to be important contributors to observed patterns of uplift (Ghelichkhan et al., 2021; Hartley et al., 2011; Parsons & Daly, 1983; Rudge et al., 2008). Surface response kernels indicate that the shallow mantle (<400 km) exerts a key role in controlling evolution of Earth's topography (Colli et al., 2016; Parsons & Daly, 1983; F. Richards, Hoggard, Crosby, et al., 2020; F. D. Richards, Hoggard, White, & Ghelichkhan, 2020). Calculated sensitivity kernels indicate that the convecting mantle directly beneath the lithosphere-asthenosphere boundary (LAB) produces the strongest contributions (from the convecting mantle) to topography (e.g., Colli et al., 2016; Ghelichkhan et al., 2021; Parsons & Daly, 1983). These results are supported by instantaneous flow models, which show, first, that topographic deflections caused by internal buoyancy anomalies have amplitudes that are inversely proportional to the depth of the anomaly (Hager & Richards, 1989). Second, they indicate that amplitudes of topography closely approximate those expected for full isostatic compensation when they are generated by buoyancy variations in the uppermost mantle (asthenosphere and lithosphere). One of the key outstanding challenges is being able to "see through" isostatic contributions from the crust and lithospheric mantle to test predictions from geodynamic models of mantle convection. Here, we first summarize geophysical and geochemical observations that indicate shallow mantle contributions to the modern elevation of the North American Western Interior. Simple isostatic calculations are then used in conjunction with those insights to

estimate contributions to net vertical motions of Cretaceous and younger marine rock from excess asthenospheric temperatures and changes to lithospheric structure.

4.1. Geophysical Features of Shallow North American Mantle

Seismic shear-wave velocities (V_S) are sensitive to temperature in the upper mantle and provide a useful guide to the thermal state of the lithosphere and asthenosphere beneath continents (e.g., Schutt & Lesher, 2006). Figure 7a shows a slice at 125 km depth through the SL2013sv shear wave velocity model and the location of Late Cretaceous to Recent mafic magmatism (Fitton et al., 1991; Klöcking et al., 2018; Roy et al., 2009; Schaeffer & Lebedev, 2014; Walker et al., 2006). Shear wave velocities show a distinctive spatial pattern, being slow in the west and fast in the east, separated by an undulating boundary. Slow velocities broadly coincide with the location of Late Cretaceous to Recent magmatism, giving complimentary indications of anomalously warm asthenosphere and thin lithospheric mantle (Ball et al., 2021).

To quantify the role of upper mantle temperatures in generating vertical lithospheric motions, the SLNAAFSA V_S tomography model of Hoggard et al. (2020)—a hybrid which embeds high-resolution regional models for North America (SL2013NA; Schaeffer & Lebedev, 2014), Africa (AF2019; Celli, Lebedev, Schaeffer, & Gaina, 2020) and the South Atlantic (SA2019; Celli, Lebedev, Schaeffer, Ravenna, & Gaina, 2020) within the global SL2013sv model of Schaeffer and Lebedev (2013)—is converted to temperature using the methodology of F. Richards, Hoggard, Crosby, et al. (2020), F. D. Richards, Hoggard, White, and Ghelichkhan (2020). This approach incorporates recent experimental parameterizations of anelasticity at seismic frequencies (Yamauchi & Takei, 2016), allowing the highly non-linear relationship between V_S and temperature at near-solidus conditions (e.g., within the asthenosphere) to be accurately constrained. Our best-fitting anelastic parameters for this model differ slightly from those quoted in Hoggard et al. (2020), due to our use of an updated oceanic lithospheric cooling model (F. Richards, Hoggard, Crosby, et al., 2020; F. D. Richards, Hoggard, White, & Ghelichkhan, 2020, instead of F. D. Richards et al., 2018). The parameters controlling the unrelaxed shear modulus, μ_U, are $\mu_0 = 75.91$ GPa, $\partial\mu/\partial T = -0.01794$, and $\partial\mu/\partial P = 2.538$ (see F. Richards, Hoggard, Crosby, et al., 2020; F. D. Richards, Hoggard, White, & Ghelichkhan, 2020, their Equation 8), while those controlling the steady-state diffusion creep viscosity and proximity to the solidus are $\eta_0 = 9.538 \times 10^{22}$ Pa s, $E_a = 4.889 \times 10^5$ J mol^{-1}, $V_a = 6.26 \times 10^{-7}$ m^3 mol^{-1}, and $\partial T_s/\partial z = 0.9309$°C km^{-1} (see F. Richards, Hoggard, Crosby, et al., 2020; F. D. Richards, Hoggard, White, & Ghelichkhan, 2020, their Equations 9 and 11). Note that this parameterization is only valid in the upper 400 km of the mantle, since calibrated material properties are appropriate for an olivine-dominated composition and do not account for phase transitions. In addition, the uppermost 50 km is excluded from our analysis to avoid errors associated with downward bleeding of crustal velocities to lithospheric depths, a problem that is particularly pronounced in continental interiors and leads to unrealistically elevated temperature predictions at shallow depths.

Calculated temperatures for the 125 km depth slice are shown in Figure 7b, and other depth slices are shown in Supporting Information S1 (Figure S7). As expected, temperatures follow the patterns of the V_S tomography model, with hottest potential temperatures in the west beneath the BR and CP reaching upwards of ~1,445°C. Mantle temperature estimates can be used to map the depth to the LAB, defined here by the 1,200°C isotherm (white dashed line in Figure 7b; Figure S8 in Supporting Information S1), which delineates a region of thinner lithosphere in the west. Note that defining the LAB by the 1,300°C isotherm, as has been done in other studies (Afonso et al., 2016), does not significantly change the observed thickness or location of significant gradients in thickness (white solid line in Figure 7b).

Figure 7c shows lithospheric thickness as defined by the 1,200°C isotherm, filtered to include only spherical harmonic degrees smaller than $l = 60$ (wavelengths >660 km; the unfiltered LAB is included in Figure S7 in Supporting Information S1). This filtering approach seeks to remove small-scale features that might be a consequence of artifacts in the underlying SLNAAFSA tomographic model. Comparison of mantle temperature and LAB depths to the observed net uplift shows that most of the uplift since the Late Cretaceous has occurred atop lithosphere that is thin compared to the interior of the continent and atop asthenosphere that is relatively warm (cf. Figures 1, 3 and 7d). The most prominent anomaly is centered on the protuberance of thicker lithosphere beneath the Colorado-Utah-Wyoming state borders, where uplift is high yet the lithosphere is thick. This region also coincides with a spatial gap in magmatism, and may indicate a more melt-depleted and viscous lithosphere.

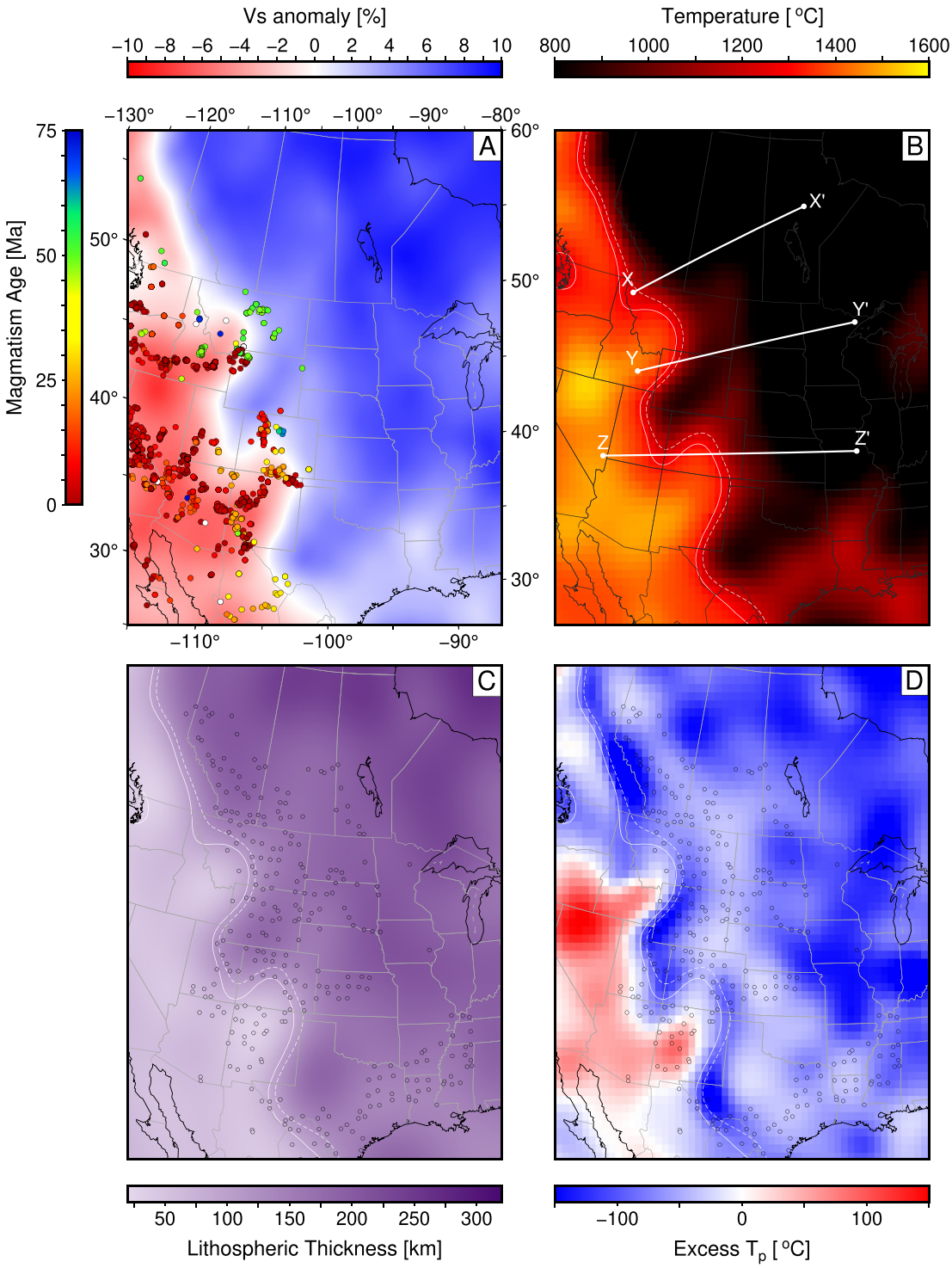

Figure 7. Shallow mantle geometries, mafic magmatism and uplift constraints. (a) Shear wave velocity anomaly at 125 km depth from Schaeffer and Lebedev (2013). Circles = magmatism colored by age from NAVDAT database with MgO >4 wt% (Walker et al., 2006). Gray lines = state/country boundaries. (b) Temperature at 125 km estimated from conversion of Schaeffer and Lebedev (2014)'s shear wave tomography model into temperature (see body text for details). White contours = 1,200°C (dashed) and 1,300°C (solid) isotherms. Labeled white lines = location of cross sections shown in Figure 8. (c) Lithospheric thickness (defined by 1,200°C isotherm), filtered to include spherical harmonic degrees less than $l = 60$ (wavelengths >660 km). Black circles = foci of binned (1 × 1°) uplift measurements (see Figure 1). (d) Excess potential temperature of shallowest 100 km beneath the base of the lithosphere. White curves = temperature contours shown in panel (b).

Figure 8 shows cross-sections of topography, mantle temperatures and lithospheric thicknesses from west to east (see Figure 7b for locations). Topographic data was extracted from the SRTM90 data set (Jarvis et al., 2008). Mantle temperatures and lithospheric thicknesses were calculated in this study (Figure 7). Crustal thicknesses were extracted from the PnUS model (Buehler & Shearer, 2016). Colored circles and squares show the present-day elevation of PBDB and stratigraphic uplift constraints, respectively. They are shown atop 100 km-wide swath profiles of elevation (see Fernandes & Roberts, 2021a, 2021b). Crustal thicknesses (black dashed lines) do not exceed 50 km and show no significant variation below topographic gradients. Assuming crustal composition does not vary significantly laterally, changes in crustal thickness alone cannot be used to explain the topographic gradient (Klöcking et al., 2018; Levandowski et al., 2018; G. G. Roberts, Paul, et al., 2012; G. G. Roberts, White, et al., 2012). On the other hand, lithospheric and asthenospheric temperatures show significant lateral variation, and consequently so does lithospheric thickness. All cross sections show an increase in lithospheric thickness to the east, accompanied by a drop in surface elevations. The magnitude of lithospheric thickness and topographic change, however, varies significantly from north to south. Cross section X–X′, crossing the Northern Rocky Mountains, shows LAB depth increasing from ∼125 to ∼225 km from east to west, concomitant with a change in the mean elevation of ∼1.6 km. Moving south to cross section Z–Z′, LAB depth increases from ∼80 km beneath the Southern Rocky Mountains to ∼200 km beneath the eastern GP, accompanied by an elevation difference of ∼2.8 km. Elevations between the CP and the Southern Rockies also have similar changes in shallow mantle temperatures and elevations.

The correspondence between upper mantle temperatures and changes in surface elevation suggests that the uppermost mantle may have played an important role in controlling the evolution of topography in the North American Western Interior. We thus combine these geophysical observations with simple isostatic models to quantify the contributions of mantle temperature and changing lithospheric thickness to the uplift history of the North American Western Interior.

4.2. Topographic Support From Asthenospheric Thermal Anomalies

We first assess contributions to topographic support from an asthenospheric channel, h, that sits directly beneath the lithosphere (see Figure S9 in Supporting Information S1). Absolute asthenospheric temperatures, T, are calculated using the SLNAAFSA tomographic model and the V_S to T conversion scheme summarized in Section 4.1 (Figures 7 and 8). Prior to calculating support, absolute temperatures are converted into potential temperatures. We do so because absolute temperatures vary as function of depth, z (strictly pressure), and we are interested in isolating contributions from thermal anomalies. Potential temperature, T_p (°C), is related to temperature, T (°C), such that

$$T_p = (T + 273)\exp\left(-\frac{\alpha g z}{C_p}\right) - 273, \tag{2}$$

where thermal expansivity $\alpha = 3.3 \times 10^{-5}$ K^{-1}, gravitational acceleration $g = 9.81$ m s^{-2}, heat capacity $C_p = 1187$ J K^{-1} kg^{-1}. Calculated temperatures are used to estimate excess potential asthenospheric temperatures, ΔT_p. They are calculated by taking the difference between the mean T_p for the layer and the background, here $T_p^\circ = 1,333$°C. Support (strictly, uplift relative to reference mantle), U—assuming isostasy prevails—can then be calculated as

$$U = \frac{h\alpha\Delta T_p}{1 - \alpha T_p^\circ}. \tag{3}$$

Note that calculated support is relatively insensitive to the choice of assumed background temperature (see, e.g., Rudge et al., 2008). Inspection of Equation 3 shows that support is sensitive to changing the thickness of the anomalously hot layer and excess temperature; doubling either doubles the support. We acknowledge that the thickness of the asthenospheric channel, h, can be defined in different ways (e.g., constant depth to the base of an asthenospheric channel, or constant thickness beneath the base of the lithosphere). Mean excess temperatures for different definitions are given in Supporting Information S1 (Figure S9). Estimated support for layers thicker than ∼100 km are likely unreliable because the isostatic approximation underpinning Equation 3 becomes increasingly less valid with depth and predicted topography begins to significantly overestimate the true amplitude of

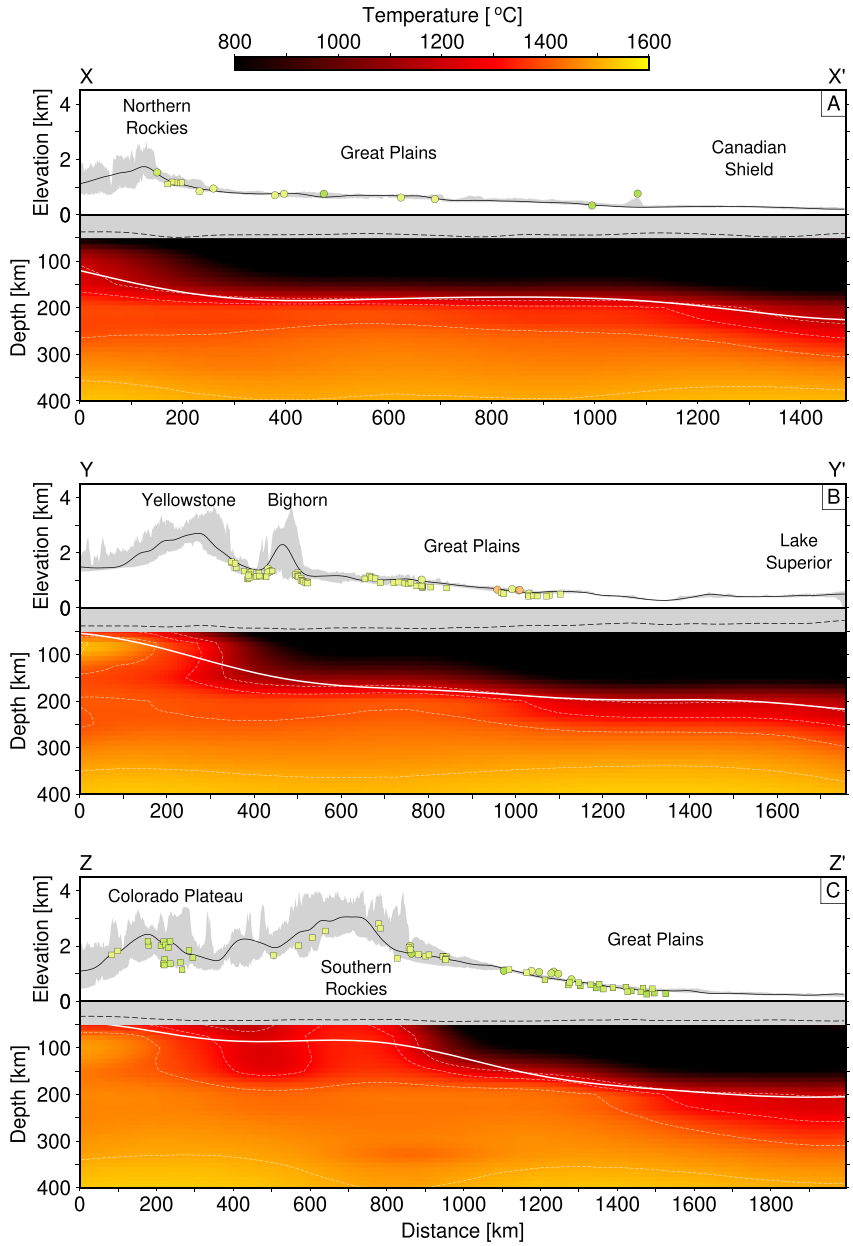

Figure 8. Cross sections through North American surface observations and calculated shallow mantle temperatures. (a) Top panel: Black curve = smoothed topography (100 km Gaussian low-pass filter) from Northern Rockies, through the Great Plains (GP) to the Canadian Shield (see line labeled X– X′ in Figure 6b); (SRTM90: Jarvis et al., 2008). Gray band = maximum and minimum topography within 100 km wide swath. Circles = uplifted marine rocks from PBDB inventory; squares = youngest recorded marine to terrestrial transitional stratigraphy; all samples are from within 100 km wide swath and are colored by age (see Figure 1). Bottom panel: Colors = temperatures calculated by converting a version of Schaeffer and Lebedev (2014)'s shear wave model (see body text for details). Thin dotted lines = isotherms in 100°C intervals. Temperatures at depths shallower than 50 km (gray band) are not shown. Black dashed line = crustal thickness from PnUS (Buehler & Shearer, 2016). Solid white line = lithosphere-asthenosphere boundary calculated from the 1,200°C isotherm smoothed by only including scales less than spherical harmonic degree $l = 60$ (wavelengths >660 km). (b, c) Cross sections through Yellowstone to Lake Superior (Y– Y′), and Colorado Plateau to the GP (Z– Z′; see Figure 6b).

asthenospheric contribution to dynamic topography. Table 1 summarizes the sensitivity of calculated support to each parameter in Equation 3 for unit adjustments. Sensitivity of all model parameters is explored in Figure 9, which we return to later after lithospheric isostatic calculations are introduced.

Table 1
Support (Strictly Uplift Relative to Reference Mantle) From Heating an Asthenospheric Layer Beneath the Lithosphere With Thickness $z_L = 200$ km and Background (Reference Mantle) Potential Temperature $T_p^\circ = 1,333°C$ by 1°C

Parameter	Reference value	δ	ΔU (km)	%
h (km)	100	±1	3.66×10^{-5}	1.01
T_p° = (°C)	1,333	±1	1.30×10^{-7}	3.6×10^{-3}
z_L (km)	200	±1	1.04×10^{-6}	0.029

We can now use stratigraphic data (Figure 3) and mantle temperatures derived from V_S tomography (Figure 7) to investigate whether the observed elevation of marine rock could be a consequence of support by asthenospheric heating. First, marine rock elevations were (spatially) averaged in 1 × 1° bins, which approximates the resolution of the shear wave tomography model. For each binned set of elevations, excess potential temperature within a 100 km thick layer beneath the base of the lithosphere was extracted from the T_p grid (Figure 7d; Supporting Information S1). Binned elevations as a function of asthenospheric potential temperature are shown in Figure 10a, with the physiographic province of each measurement indicated by color (see Figure 1b for locations and colors). The distribution of elevations is broadly uniform between 0.5 and 2 km. The distribution of potential temperatures is unimodal, with cool mantle temperatures in the shallowest 100 km beneath the lithosphere (mostly 1,200 < T_p < 1,300°C), with respect to assumed background mantle temperature T_p = 1,333°C. Few locations beneath the CP and BR have calculated shallow mantle potential temperature anomalies exceeding 1,333°C, in agreement with estimates of potential temperatures for the region from basalt geochemistry (Klöcking et al., 2018).

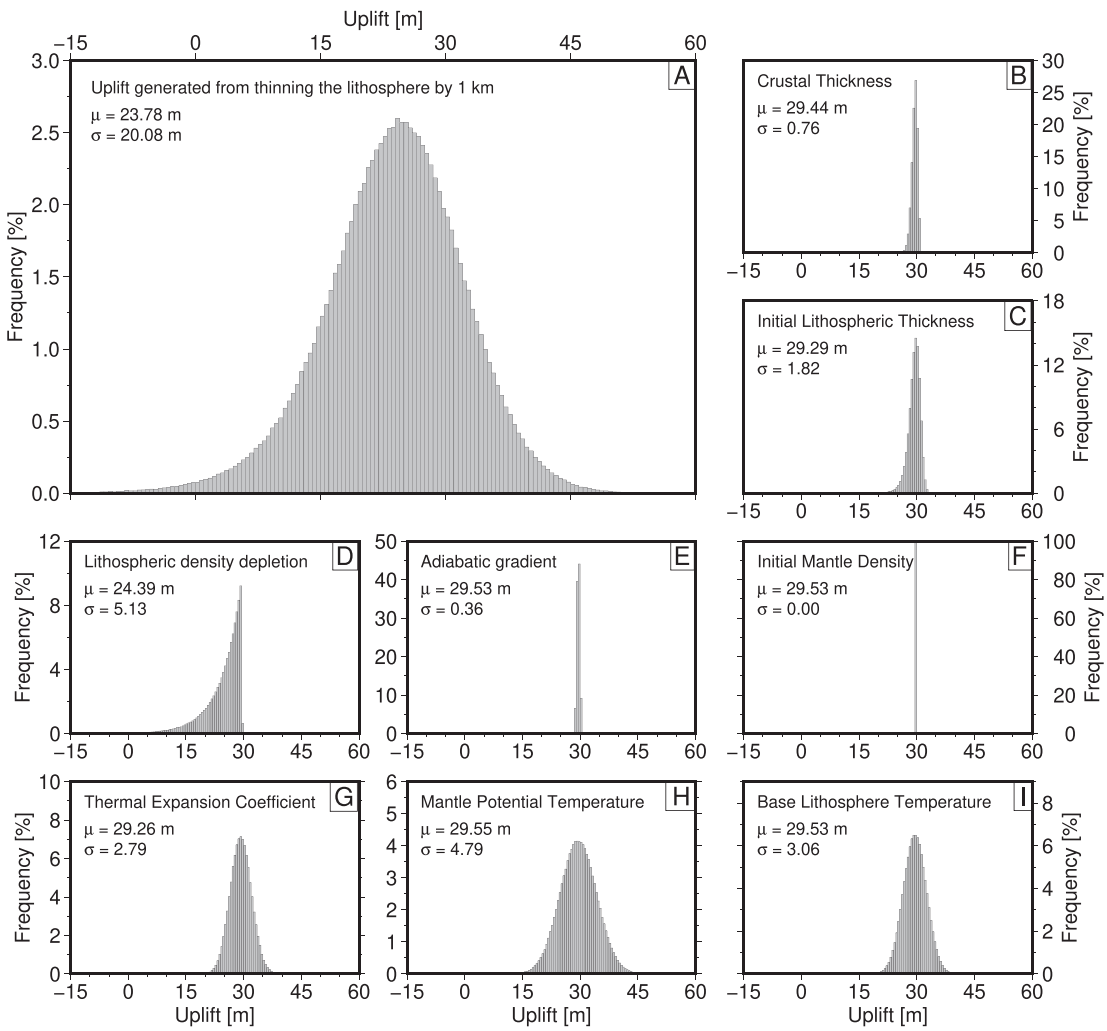

Figure 9. Sensitivity of calculated uplift following 1 km of lithospheric thinning (a) Distribution (mean = μ, standard deviation = σ) of calculated isostatic uplift generated by Monte Carlo simulation varying all parameters in Equation 4 simultaneously: crustal thickness, initial lithospheric thickness, lithospheric density depletion, adiabatic gradient, initial mantle density, thermal expansion coefficient, mantle potential temperature, and temperature at the base of the lithospheric mantle. Variance of parameters included in this test are indicated in following panels. (b)–(i) Calculated distributions of uplift that arise by holding all parameters fixed except one, annotated in each panel.

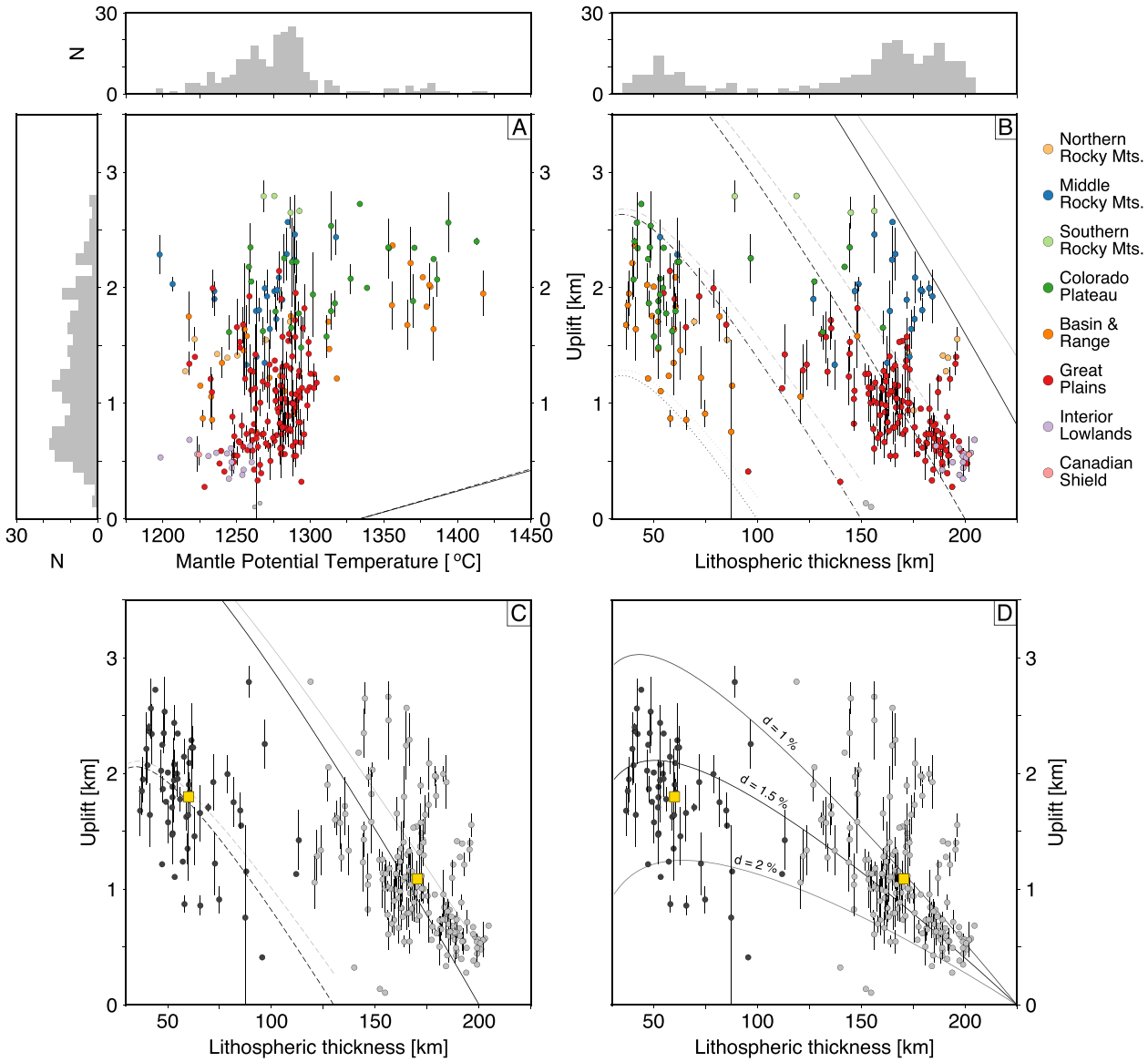

Figure 10. Assessing the role of lithospheric thinning and asthenospheric temperatures for generating observed uplift. (a) Uplift measured from stratigraphic observations compared to calculated mean potential temperatures of a 100 km thick asthenospheric channel beneath the base of the lithosphere. Circles = mean values in $1 \times 1°$ bins; error bars = 1σ of uplift measurements in bin. Potential temperatures were extracted from thermal model shown in Figures 6 and 7 (see body text for details). Circles are colored according to location (see legend); post-Cretaceous uplift data from the Gulf of Mexico coastal plain are not included. Histograms atop and aside main panel show distributions of calculated potential temperatures and uplift measurements, respectively. Lines = predicted isostatic uplift for anomalously warm 100 km (solid) or 200 km (dashed) thick asthenospheric channels (see body text). (b) Uplift measurements in $1 \times 1°$ bins compared to lithospheric thickness estimates shown in Figure 6C. Black lines = predicted uplift for thermally equilibrated thinning of lithosphere with initial thicknesses of 250 (solid), 200 (dashed), 150 (dot-dashed), or 100 (dotted) km. Nearby gray lines are for thinning without thermal equilibration. (c) Uplift as a function of lithospheric thickness, colored by cluster calculated using k-means clustering algorithm. Yellow squares = cluster centroids. Centroid values are consistent with (thermally equilibrated or disequilibrated) thinning of lithosphere with initial thicknesses of 130 km (black and gray dotted lines) or 200 km (back and gray dashed lines). (d) Black lines show thermally equilibrated thinning of lithosphere with initial thickness of 225 km with different degrees of lithospheric density depletion.

Equation 3 can be used to explore whether observed elevations can be explained by asthenospheric heating alone. The solid black line in Figure 10a shows support (strictly uplift, Equation 3) predicted from heating a 100 km thick asthenospheric layer located immediately beneath the LAB. The isostatic calculation predicts no more than 500 m of uplift from a layer with T_p = 1,450°C if heating from a background mantle potential temperature of 1,333°C is assumed. If the background mantle temperature is assumed to be significantly cooler, for example, 1,200°C, maximum predicted uplift is still less than 1 km. These results indicate that isostatic support from

Table 2
Calculated Variance of Lithospheric Isostatic Support, ΔU, From a Systematic Sweep of Modified Parameter Values (From Reference Values Indicated in Second Column)

Parameter	Reference value	δ	ΔU (km)	%
t_{cc}	40	±1	1.70×10^{-4}	0.65
d	0	+0.01	-1.0245×10^{-2}	−39.3
dT/dz	0.44	±0.01	5.9×10^{-5}	0.23
T_p	1,333	±1	4.7×10^{-5}	0.18
T_{bl}	100	±1	3.2×10^{-5}	0.12

Note. Variance of parameter values, δ, are given in third column. Parameters: crustal thickness (t_{cc}, km), lithospheric density depletion factor (d), geothermal gradient (dT/dz, °C km^{-1}), mantle potential temperature (T_p, °C), temperature of thermal boundary layer (T_{bl}, °C). % indicates percentage difference to calculated support for reference lithosphere (U = 0.03 km). Sensitivity analysis for thinning 200 km-thick lithosphere can be found in Supporting Information S1.

heating of even an anomalously cool asthenospheric mantle alone cannot explain the 2–3 km of observed elevations. At most, ∼1 km of uplift of the CP and BR can be explained by warming of initially cool asthenospheric mantle. Other obvious contributors to isostatic support are lithospheric thicknesses and densities. Thus, in the following subsection we assess the consequences of thermally equilibrated and disequilibrated lithosphere for generating observed patterns of uplift.

4.3. Relations Between the Lithosphere and Elevation of Marine Stratigraphy

We examine contributions from thermally equilibrated and disequilibrated lithosphere with a view to assessing the range of topographic support that lithospheric mantle could provide to topography. We discuss their geologic implications, with regards to histories of lithospheric thinning, in Section 5. Assuming isostasy prevails, support as a function of thermally equilibrated lithospheric thinning, $U(\Delta t_L)$, is given by

$$U(\Delta t_L) = \frac{1}{\rho_a}\left[t_{L_i}(\rho_{L_i} - \rho_a) + t_{TBL_i}(\rho_{TBL_i} - \rho_a) + (t_{L_i} - \Delta t_L)(\rho_a - \rho_{L_f}) + t_{TBL_f}(\rho_a - \rho_{TBL_f})\right] \quad (4)$$

where t_{L_i} and is the initial lithospheric thickness, t_{TBL_i} and t_{TBL_f} are the initial and final thickness of the thermal boundary layer, respectively. Density of asthenospheric mantle is given by ρ_a, and the initial and final densities of lithospheric mantle and thermal boundary layer are given by ρ_{L_i}, ρ_{L_f}, ρ_{TBL_i}, ρ_{TBL_f}, respectively. The depth to the base of the thermal boundary layer, z_{TBL}, is defined as a linear function of the thickness of the lithosphere, and is given by

$$z_{TBL} = (1.678 z_{L_i}) - 5.472, \quad (5)$$

where z_{L_i} is the depth to the base of the lithosphere. This relationship is derived by analyzing the correspondence between the depth to the 1,200°C isotherm inferred from V_S-derived geothermal profiles and the depth to the base of the thermal boundary layer obtained by fitting steady-state geotherms to these V_S-based temperature predictions (see Text S3 and Equation S1 in Hazzard et al., 2023).

In an idealized case, density of the lithospheric mantle, thermal boundary layer and asthenospheric mantle are taken to be a function of temperature. Mantle density, ρ_m, is calculated as

$$\rho_m = \rho_\circ(1 - \alpha\overline{T_m}), \quad (6)$$

where $\rho_\circ$ is the reference mantle density at standard temperature and pressure (3.33 Mg m^{-3}), α is the mantle thermal expansivity, and $\overline{T_m}$ is the average temperature of the mantle layer. For lithospheric mantle densities, ρ_L, compositional variation can be included as $(1-d)\rho_\circ(1-\alpha\overline{T_a})$ where d is a lithospheric density depletion factor between 0 and 1. The temperature of the lithospheric mantle is calculated assuming a linear geothermal gradient from the surface, here set to 0°C, to the base of the lithosphere, defined at the 1,200°C isothermal surface. The temperature of the thermal boundary layer is calculated assuming an upper bounding temperature of 1,200°C and a basal temperature calculated assuming an adiabatic gradient defined by Equation 2. Similarly, temperature of the asthenospheric mantle is calculated using the same adiabatic gradient.

These equations can be used to propagate uncertainties and to assess the sensitivity of calculated support to the properties of the lithosphere. Table 2 shows sensitivity of calculated support to unit adjustment, δ, of each parameter. Calculated support is most sensitive to density depletion.

To develop greater statistical insight, we performed a Monte-Carlo error analysis. One million calculations of isostatic support in response to thinning the lithosphere by 1 km, and unit adjustments to all other parameters, were performed. All parameters were varied within specified ranges and have well-defined (mostly normal)

distributions (Figure 9). Crustal thickness was varied such that the mean and variance reflected values observed within the North American Western Interior (mean = 40 km, standard deviation = 10 km; Buehler & Shearer, 2016). Initial lithospheric thickness was also assigned a mean of 150 km and standard deviation of 30 km, reflecting the vertical resolution of the SLNAAFSA tomography model. The thermal expansion coefficient, 3.3×10^{-5} K^{-1}, was assigned a 10% standard deviation, which encompasses the predicted range of values as reported by Bouhifd et al. (1996) and Katsura et al. (2009). Similarly, the temperature at the base of the lithosphere, 1,200°C, adiabatic gradient, simplified to 4.44°C/km, and reference mantle density, 3.33 Mg m^{-3}, were all assumed to have a standard deviation of 10%. Mantle potential temperature, 1,333°C, was assigned a standard deviation of 100°C, which encompasses a range of values for 'standard' mantle (Parsons & Sclater, 1977). Lithospheric density depletion was assigned an exponential distribution such that 50% of tested densities are between 3.3 and 3.29 Mg m^{-3}, 30% are between 3.29 and 3.27 Mg m^{-3}, and 20% are between 3.27 and 3.25 Mg m^{-3} Figure 9 shows uplift following 1 km of lithospheric thinning; First, all uncertainties were incorporated by varying all parameters simultaneously, shown in Figure 9a, while Figures 9b–9i do the same calculation while holding all variables fixed except one.

The results show that there is a well-defined peak in predicted support centered at ~24 m per km thinning, with a large uncertainty. Most of the uncertainty is a consequence of uncertain background mantle potential temperatures, thermal expansion coefficient values, temperatures at the base of the lithosphere, and mantle density depletion factors. If the density of lithospheric mantle is known, the uncertainty in predicted isostatic support is significantly reduced (see Figure 9). We now explore how the histories of uplift inferred from the inventory of uplifted marine rock can be used to assess the history of shallow isostatic support. We seek to quantify the roles asthenospheric temperature anomalies and changes to lithospheric architecture played in post-Cretaceous uplift of North America.

5. Exploring Shallow Isostatic Origins for the History of Observed Uplift

First, we examine the consequences of assuming that lithospheric thinning alone can explain observed patterns of uplift. Thermally equilibrated lithospheric thinning requires the thermal boundary layer (between the lithosphere and convecting mantle) to be present during thinning. In contrast, thermally disequilibrated thinning implies that the thermal boundary layer is removed instantaneously during thinning and replaced by asthenospheric mantle, creating a discontinuity in temperature across the LAB. We test these two end-member scenarios to place lower and upper bounds on calculated uplift. Calculated uplift from thinning of thermally equilibrated and disequilibrated lithosphere with initial thicknesses (at 0 uplift) of 150, 200, and 250 km are shown in Figure 10b, colored by geographic province (Equation 4). Uplift of the GP and most of the Middle Rocky Mountains can be explained by thinning initially thick (>200 km) lithosphere, while uplift of the CP and BR can be explained by thinning of an originally relatively thin (<150 km) lithosphere.

The distribution of calculated lithospheric thicknesses are broadly bimodal (see histogram atop Figure 10b). Thus, to simplify our approach, we estimate uplift from lithospheric thinning for only these two modes. We do so by back-projecting the centroids of lithospheric thickness-uplift pairs along equilibrium and disequilibrium lithospheric thinning trajectories (Figure 10c: solid, dashed gray and black lines). The centroids were identified using a *k-means* algorithm (see Figure S10 in Supporting Information S1). Figures 10c and 10d shows the results of the *k-means* clustering algorithm. The number of clusters is chosen a priori by calculating the total within-cluster sum of squared distances (WCSS; see Supporting Information S1). The first centroid is (60 km, 1.8 km) and contains localities mostly within the CP, BR, and parts of the Middle and Northern Rocky Mountains. The second centroid is (170 km, 1.1 km), at the center of a cluster encompassing localities from the Canadian Shield (CS) and IL. Calculated initial lithospheric thicknesses for the two clusters are 130 and 200 km. This result can be explained by thinning of lithosphere beneath the CP and BR from 130 km to 80–70 km. The second cluster contains loci atop lithosphere that progressively thins to the West by as much as 100 km. These results indicate that the tilting of the GP, with highest uplift in the Southern and Middle Rocky Mountains, can be explained by thinning of lithosphere that was initially ~200 km thick.

Second, we explore an alternative explanation in which lithosphere with different densities are thinned. Estimates of lithospheric mantle density from gravity modeling suggests that cratonic lithosphere, present beneath the eastern region of our study area, has a density depleted by 30–70 kg m^{-3} (Mooney & Kaban, 2010). Lamb et al. (2020) proposed that the lithosphere here is depleted by 20–40 kg m^{-3} compared to the asthenospheric

mantle. Figure 10d shows thinning trajectories for a lithosphere that is initially 225 km thick (e.g., the modern CS). It shows results for different assumed reductions in density. A useful rule of thumb is that a 1% reduction lowers density by ≈36 kg m^{-3}. Assuming that lithospheric mantle densities were 1%–2% depleted (prior to thinning) implies that up to 150 km of thinning, from an initial thickness of 250 km (across the entire domain), would be required to explain observed patterns of uplift. That would constitute a major geological event that could be tested in the future using independent observations of, for example, heat flow and xenolith-derived paleo-lithospheric thicknesses, and more granular uplift histories.

6. Discussion

There now exists a considerable body of quantitative paleogeographic, uplift and subsidence observations with which surface deflections predicted by geodynamic models of the mantle can be tested (e.g., PBDB, Macro-Strat; Figures 1–3). In this study, we augmented marine fossil assemblages recorded in the PBDB with stratigraphic information to test the timing, amplitude and distribution of dynamic topography of Western North America predicted by the models presented by Müller et al. (2018).

Their Model M1 does not explain post-Cretaceous net uplift (it is lower by up to a factor of 2; Figure 5a). It does however broadly predict paleo-water depths that are consistent with estimates from the fossil record (Figure 5b). In contrast, models M2–M4 broadly reproduce amplitudes of net post-Cretaceous uplift (Figure 5c), but do not explain observed patterns of Cretaceous paleo-bathymetry. In particular, predicted dynamic drawdown implies a much deeper depth for the Western Interior Seaway than its fossil assemblages indicate (e.g., Figure 5d). We note that Müller et al. (2018)'s preferred model is M7, since it yields realistic continental flooding histories. However, the model explicitly suppresses plume formation, which probably reduces similarity to actual mantle convection. We note that calculated net dynamic topography in Model 7 is up to a factor of 3 lower than observed net uplift. Similarly, these models do not explain subsidence histories of basins in the Western Interior inferred by back-stripping stratigraphy (Figure 6). As Müller et al. (2018) point out, an obvious source of these discrepancies is the lack of contributions to topographic support in these models from the uppermost few hundred kilometers. We addressed this issue as follows.

Recent shear wave tomographic models were used to estimate lithospheric and asthenospheric temperatures, and thence structure (Figures 7–10). This information was combined with simple isostatic calculations to assess whether shallow isostatic contributions can explain observed patterns of net uplift. Heating shallow asthenospheric mantle alone is unlikely to be sufficient for explaining observed net uplift. Maximum amplitudes predicted from heating are too low for reasonable parameter values (Figure 10a). In contrast, thinning lithospheric mantle (whether depleted or of variable initial thickness) can, on its own explain, observed patterns of uplift (Figures 10c and 10d). This proposed lithospheric thickness evolution is independently supported by petrological modeling of eclogite xenoliths from the CP, which suggests that up to 80 km of shear-driven removal of sub-continental lithospheric mantle occurred between Cretaceous and Eocene times, from an initial lithospheric thickness of 200 to 120–130 km (Hernández-Uribe & Palin, 2019). In addition, petrological analysis of garnet inclusions in peridotite xenoliths of the same region suggest an additional ∼50 km of lithospheric thinning, from ∼130 to ∼80 km, from Eocene to present (Hunter & Smith, 1981; Riter & Smith, 1996). These results are also consistent with histories of sub-lithospheric support of Western North America inferred from melt histories of mafic rocks in the region (e.g., Ball et al., 2021).

Figure 11 demonstrates an attempt to reconcile predicted contributions to net uplift of Western North America. They show the "targets," that is, net uplift estimated using fossil assemblages and associated corrections for paleo-water depth and sea level. Also shown are estimated contributions to net uplift from the three sources considered in this paper. First, contributions from the deep mantle are extracted from Müller et al. (2018)'s Model M5. Second, isostatic asthenospheric support is estimated from excess temperatures calculated using shear wave tomography (Figures 7 and 8; Equation 3). Finally, the residual is attributed to lithospheric thinning, which can be compared to Figure 10. The two examples shown include a locality from the Book Cliffs in Western North America and from eastern Iowa on the GP. These results emphasize the importance of constraining lithospheric thicknesses and densities for determining the history of net uplift and thus for using such observations to determine the history of mantle convection.

We finish by noting that a variety of alternative approaches to predict dynamic support could be tested in future work using the uplift and subsidence histories developed in this paper. For instance, they could be used to test

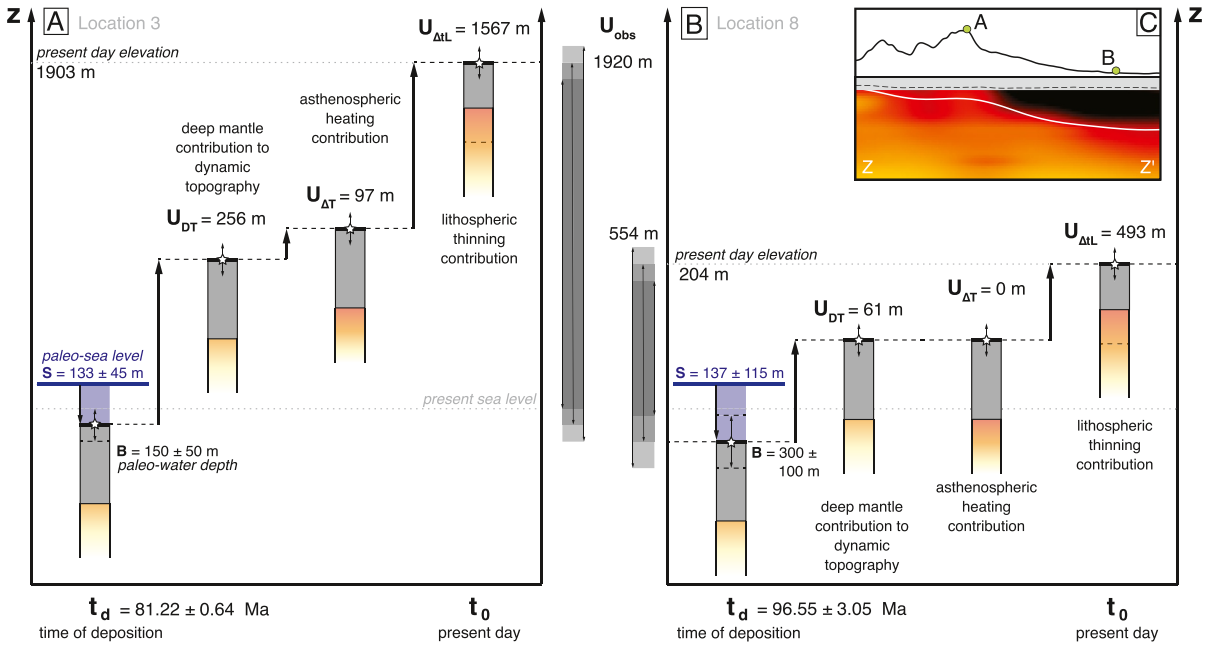

Figure 11. Reconciling dynamic and isostatic drivers of uplift in the North American Western Interior. These schematics incorporate dynamic topography predicted by mantle convection simulations (Model M5; Figure 4), and estimated additional asthenospheric heating and lithospheric thinning required to generate observed uplift (see Figure 10 and body text for details). (a) Uplift of the Book Cliffs (Location 3: Figures 2 and 3). Note that the lithospheric thinning required to match observed uplift is significantly less if predictions from models M2–M4 are considered. (b) Uplift in eastern Iowa (Location 8: Figure 3). (c) Schematic cross section across the study region showing the positions of these examples (see Figure 7B: Z–Z′ for location).

predictions from analytic solutions of the equations of motion, models that assimilate tomographic information, adjoint inverse methodologies, and alternative parameterizations of, for example, plate motion histories, surface boundary conditions, mantle composition and viscosity, as well as new approaches for incorporating lithosphere-asthenosphere interactions into geodynamic simulations (e.g., Davies et al., 2023; Ghelichkhan et al., 2021; Hayek et al., 2021; Young et al., 2022). Refining knowledge of lithospheric densities and structure is likely to remain a fundamental concern in the quantification of sub-plate support of topography and thus in the search for the history of mantle convection.

7. Conclusions

Histories of mantle convection and their role in generating vertical motions of Earth surface are of general interest. That a considerable body of mantle convection simulations predict differing surface deflection histories indicates that identifying optimal models using independent geologic observations is likely to be a fruitful endeavor. In this paper we combine digital inventories of paleobiological data with stratigraphic information to explore origins of western North American topography. We demonstrate that geodynamic simulations that exclude the uppermost few hundred kilometers of the mantle cannot, on their own, reproduce observed patterns of vertical motions. We also demonstrate that excess asthenospheric temperatures, on their own, are insufficient for explaining net support of Western North American topography. Since crustal thicknesses across this region appear to be broadly similar we instead, turn to modification of lithospheric mantle as a source of post-Cretaceous net uplift. We demonstrate that changes to lithospheric thickness and depletion could explain observed patterns of uplift, and that this proposed mechanism is consistent with independent petrological constraints on lithospheric evolution. These results emphasize the importance of determining the properties (e.g., densities and structure) of the lithosphere (especially the lithospheric mantle) and its modification by the convecting mantle if we are to understand how the convecting mantle impacts surface processes and vice versa.

Data Availability Statement

All data used in this publication are accessible through online, open-access data repositories. Dynamic topography models from Müller et al. (2018) can be accessed through the open data repository https://www.earthbyte.org/global-dynamic-topography-models/. Database for uplift measurements from paleobiological data, from Fernandes and Roberts (2021a, 2021b), can be accessed through the open data repository https://doi.org/10.1130/GSAB.S.12939470. All other data sets used in this research can be accessed in the following data repository: https://doi.org/10.5281/zenodo.10212951 (Fernandes, 2023).

Acknowledgments
We thank two anonymous reviewers and the Associate Editor for their help. VMF was supported by NERC Grant NE/T012501/1.

References

Afonso, J. C., Moorkamp, M., & Fullea, J. (2016). Imaging the lithosphere and upper mantle. In M. Moorkamp, P. G. Lelièvre, N. Linde, & A. Khan (Eds.), *Integrated imaging of the Earth: Geophysical monograph series*. https://doi.org/10.1002/9781118929063.ch10

Athy, L. F. (1930). Density, porosity, and compaction of sedimentary rocks. *AAPG Bulletin*, *141*, 1–24. https://doi.org/10.1306/3D93289E-16B1-11D7-8645000102C1865D

Audet, P. (2014). Toward mapping the effective elastic thickness of planetary lithospheres from a spherical wavelet analysis of gravity and topography. *Physics of the Earth and Planetary Interiors*, *226*, 48–82. https://doi.org/10.1016/j.pepi.2013.09.011

Austermann, J., Mitrovica, J. X., Huybers, P., & Rovere, A. (2017). Detection of a dynamic topography signal in last interglacial sea-level records. *Science Advances*, *3*(7), e1700457. https://doi.org/10.1126/sciadv.1700457

Austermann, J., Pollard, D., Mitrovica, J. X., Moucha, R., Forte, A. M., DeConto, R. M., et al. (2015). The impact of dynamic topography change on Antarctic ice sheet stability during the mid-Pliocene warm period. *Geology*, *43*(10), 927–930. https://doi.org/10.1130/G36988.1

Ball, P. W., White, N. J., Maclennan, J., & Stephenson, S. N. (2021). Global influence of mantle temperature and plate thickness on intraplate volcanism. *Nature Communications*, *12*(2045), 2045. https://doi.org/10.1038/s41467-021-22323-9

Barnett-Moore, N., Hassan, R., Müller, R. D., Williams, S. E., & Flament, N. (2017). Dynamic topography and eustasy controlled the paleogeographic evolution of northern Africa since the mid-Cretaceous. *Tectonics*, *36*(5), 929–944. https://doi.org/10.1002/2016TC004280

Becker, J. J., Sandwell, D. T., Smith, W. H. F., Braud, J., Binder, B., Depner, J., et al. (2009). Global bathymetry and elevation data at 30 arc seconds resolution: SRTM30_PLUS. *Marine Geodesy*, *32*(4), 355–371. https://doi.org/10.1080/01490410903297766

Bessin, P., Guillocheau, F., Robin, C., Braun, J., Bauer, H., & Schroetter, J.-M. (2017). Quantification of vertical movement of low elevation topography combining a new compilation of global sea-level curves and scattered marine deposits (Armorican Massif, western France). *Earth and Planetary Science Letters*, *470*, 25–36. https://doi.org/10.1016/j.epsl.2017.04.018

Blum, M., & Pecha, M. (2014). Mid-Cretaceous to Paleocene North American drainage reorganization from detrital zircons. *Geology*, *42*(7), 607–610. https://doi.org/10.1130/G35513.1

Bond, G. (1976). Evidence for continental subsidence in North America during the Late Cretaceous global submergence. *Geology*, *4*(9), 557–560. https://doi.org/10.1130/0091-7613(1976)4<557:EFCSIN>2.0.CO;2

Bouhifd, M. A., Andrault, D., Fiquet, G., & Richet, P. (1996). Thermal expansion of forsterite up to the melting point. *Geophysical Research Letters*, *23*(10), 1143–1146. https://doi.org/10.1029/96GL01118

Buehler, J. S., & Shearer, P. M. (2016). Uppermost mantle seismic velocity structure beneath USArray. *Journal of Geophysical Research*, *121*(1), 436–448. https://doi.org/10.1002/2016JB013265

Bunge, H. P., & Baumgardner, J. R. (1995). Mantle convection modeling on parallel virtual machines. *Computers in Physics*, *9*(2), 207–215. https://doi.org/10.1063/1.168525

Celli, N. L., Lebedev, S., Schaeffer, A. J., & Gaina, C. (2020). African Cratonic lithosphere carved by mantle plumes. *Nature Communications*, *11*(1), 1–10. https://doi.org/10.1038/s41467-019-13871-2

Celli, N. L., Lebedev, S., Schaeffer, A. J., Ravenna, M., & Gaina, C. (2020). The upper mantle beneath the South Atlantic Ocean, South America and Africa from waveform tomography with massive data sets. *Geophysical Journal International*, *221*(1), 178–204. https://doi.org/10.1093/gji/ggz574

Chamberlain, C. P., Mix, H. T., Mulch, A., Hren, M. T., Kent-Corson, M. L., Davis, S. J., et al. (2012). The Cenozoic climatic and topographic evolution of the western north American Cordillera. *American Journal of Science*, *312*(2), 213–262. https://doi.org/10.2475/02.2012.05

Cobban, W. A., Walaszczyk, I., Obradovich, J. D., & McKinney, K. C. (2006). A USGS zonal table for the upper Cretaceous Middle Cenomanian–Maastrichtian of the western interior of the United States based on ammonites, Inoceramids, and radiometric ages. Technical report.

Colli, L., Ghelichkhan, S., & Bunge, H. P. (2016). On the ratio of dynamic topography and gravity anomalies in a dynamic Earth. *Geophysical Research Letters*, *43*(6), 2510–2516. https://doi.org/10.1002/2016GL067929

Conway-Jones, B. W., & White, N. (2022). Paleogene buried landscapes and climatic aberrations triggered by mantle plume activity. *Earth and Planetary Science Letters*, *593*, 117644. https://doi.org/10.1016/j.epsl.2022.117644

Cox, K. G. (1989). The role of mantle plumes in the development of continental drainage patterns. *Nature*, *342*(6252), 873–877. https://doi.org/10.1038/342873a0

Cross, T. A. (1986). Tectonic controls of foreland basin subsidence and Laramide style deformation, western United States. In P. A. Allen & P. Homewood (Eds.), *Foreland basins*. https://doi.org/10.1002/9781444303810.ch1

Cross, T. A., & Piliger, R. H. (1978). Tectonic controls of late Cretaceous sedimentation, western interior, USA. *Nature*, *247*, 653–657. https://doi.org/10.1038/274653a0

Crough, S. T. (1983). Hotspot swells. *Annual Review of Earth and Planetary Sciences*, *11*(1), 165–193. https://doi.org/10.1146/annurev.ea.11.050183.001121

Czarnota, K., Roberts, G. G., White, N. J., & Fishwick, S. (2014). Spatial and temporal patterns of Australian dynamic topography from River Profile Modeling. *Journal of Geophysical Research: Solid Earth*, *119*(2), 1384–1424. https://doi.org/10.1002/2013JB010436

Davies, D. R., Ghelichkhan, S., Hoggard, M. J., Valentine, A. P., & Richards, F. D. (2023). Observations and models of dynamic topography: Current status and future directions. *Dynamics of Plate Tectonics and Mantle Convection*, 223–269. https://doi.org/10.1016/B978-0-323-85733-8.00017-2

DeCelles, P. G. (1994). Late Cretaceous-Paleocene synorogenic sedimentation and kinematic history of the Sevier thrust belt, northeast Utah and southwest Wyoming. *GSA Bulletin*, *106*(1), 32–56. https://doi.org/10.1130/0016-7606(1994)106<0032:LCPSSA>2.3.CO;2

DeCelles, P. G. (2004). Late Jurassic to Eocene evolution of the Cordilleran thrust belt and foreland basin system, Western U.S.A. *American Journal of Science*, *304*(February), 105–168. https://doi.org/10.2475/ajs.304.2.105

Dickinson, W. R. (2004). Evolution of the North American Cordillera. *Annual Review of Earth and Planetary Sciences*, *32*(1), 13–45. https://doi.org/10.1146/annurev.earth.32.101802.120257

Dickinson, W. R., Klute, M. A., Hayes, M. J., Janecke, S. U., Lundin, E. R., McKittrick, M. A., & Olivares, M. D. (1988). Paleogeographic and paleotectonic setting of Laramide sedimentary basins in the central Rocky Mountain region. *GSA Bulletin*, *100*(7), 1023–1039. https://doi.org/10.1130/0016-7606(1988)100<1023:PAPSOL>2.3.CO;2

Ding, X., Dávila, F. M., & Lithgow-Bertelloni, C. (2023). Mechanisms of subsidence and uplift of Southern Patagonia and offshore basins during slab window formation. *Geochemistry, Geophysics, Geosystems*, *24*(5), e2022GC010844. https://doi.org/10.1029/2022GC010844

Faccenna, C., Glišović, P., Forte, A., Becker, T. W., Garzanti, E., Sembroni, A., & Gvirtzman, Z. (2019). Role of dynamic topography in sustaining the Nile River over 30 million years. *Nature Geoscience*, *12*(12), 1012–1017. https://doi.org/10.1038/s41561-019-0472-x

Fenneman, N. (1928). Physiographic divisions of the United States. *Annals of the Association of American Geographers*, *18*(4), 261–353. https://doi.org/10.2307/2560726

Fernandes, V. M. (2023). Open research datasets—Testing mantle convection simulations with paleobiology and other stratigraphic observations: Examples from western North America [Dataset]. *Zenodo*. https://doi.org/10.5281/zenodo.10212951

Fernandes, V. M., & Roberts, G. G. (2021a). Cretaceous to recent net continental uplift from paleobiological data: Insights into sub-plate support. *Geological Society of America Bulletin*, *133*(5–6), 1217–1236. https://doi.org/10.1130/B35739.1

Fernandes, V. M., & Roberts, G. G. (2021b). Supplemental Material: Cretaceous to recent net continental uplift from paleobiological data: Insights into sub-plate support [Dataset]. *Geological Society of America Journal Contribution*. https://doi.org/10.1130/GSAB.S.12939470.v1

Fernandes, V. M., Roberts, G. G., White, N. J., & Whittaker, A. C. (2019). Continental-scale landscape evolution: A history of North American topography. *Journal of Geophysical Research: Earth Surface*, *124*(11), 2689–2722. https://doi.org/10.1029/2018JF004979

Fitton, J. G., James, D., & Leeman, W. P. (1991). Basic magmatism associated with Late Cenozoic extension in the western United States: Compositional variations in space and time. *Journal of Geophysical Research*, *96*(B8), 13693–13711. https://doi.org/10.1029/91JB00372

Flament, N., Gurnis, M., & Müller, R. D. (2013). A review of observations and models of dynamic topography. *Lithosphere*, *52*(2), 189–210. https://doi.org/10.1130/L245.1

Flament, N., Williams, S., Müller, R., Gurnis, M., & Bower, D. (2017). Origin and evolution of the deep thermochemical structure beneath Eurasia. *Nature Communications*, *8*(1), 14164. https://doi.org/10.1038/ncomms14164

Flowers, R. M., Ault, A. K., Kelley, S. A., Zhang, N., & Zhong, S. (2012). Epeirogeny or Eustasy? Paleozoic-Mesozoic vertical motion of the North American continental interior from thermochronometry and implications for mantle dynamics. *Earth and Planetary Science Letters*, *317–318*, 436–445. https://doi.org/10.1016/j.epsl.2011.11.015

Flowers, R. M., & Farley, K. A. (2012). Apatite ^{4}He/^{3}He and (U-Th)/He Evidence for an Ancient Grand Canyon. *Science*, *338*(6114), 1616–1619. https://doi.org/10.1126/science.1229390

Flowers, R. M., Wernicke, B. P., & Farley, K. A. (2008). Unroofing, incision, and uplift history of the southwestern Colorado Plateau from apatite (U-Th)/He thermochronometry. *GSA Bulletin*, *120*(5–6), 571–587. https://doi.org/10.1130/B26231.1

Forte, A. M. (2000). Seismic-geodynamic constraints on mantle flow: Implications for layered convection, mantle viscosity, and seismic anisotropy in the deep mantle. In S. I. Karato, A. Forte, R. Liebermann, G. Masters, & L. Stixrude (Eds.), *Earth's deep interior: Mineral physics and tomography from the atomic to the global scale. American geophysical Union-Geophysical monograph series* (Vol. 117, pp. 3–36). https://doi.org/10.1029/GM117p0003

Forte, A. M., Mitrovica, J. X., Moucha, R., Simmons, N. A., & Grand, S. P. (2007). Descent of the ancient Farallon slab drives localized mantle flow below the New Madrid seismic zone. *Geophysical Research Letters*, *34*(4), L04308. https://doi.org/10.1029/2006GL027895

Forte, A. M., Moucha, R., Simmons, N. A., Grand, S. P., & Mitrovica, J. X. (2009). Deep-mantle contributions to the surface dynamics of the North American continent. *Tectonophysics*, *481*(1–4), 3–15. https://doi.org/10.1016/j.tecto.2009.06.010

Forte, A. M., Quéré, S., Moucha, R., Simmons, N. A., Grand, S. P., Mitrovica, J. X., & Rowley, D. B. (2010). Joint seismic–geodynamic-mineral physical modelling of African geodynamics: A reconciliation of deep-mantle convection with surface geophysical constraints. *Earth and Planetary Science Letters*, *295*(3–4), 329–341. https://doi.org/10.1016/j.epsl.2010.03.017

Galloway, W. E., Whiteaker, T. L., & Ganey-Curry, P. (2011). History of Cenozoic North American drainage basin evolution, sediment yield, and accumulation in the Gulf of Mexico basin. *Geosphere*, *7*(4), 938–973. https://doi.org/10.1130/GES00647.1

Gani, R. M., Ranson, A., Cross, D. B., Hampson, G. J., Gani, N. D., & Sahoo, H. (2015). Along-strike sequence stratigraphy across the Cretaceous shallow marine to coastal-plain transition, Wasatch Plateau, Utah, U.S.A. *Sedimentary Geology*, *325*, 59–70. https://doi.org/10.1016/j.sedgeo.2015.05.003

Ghelichkhan, S., Bunge, H., & Oeser, J. (2021). Global mantle flow retrodictions for the early Cenozoic using an adjoint method: Evolving dynamic topographies, deep mantle structures, flow trajectories and sublithospheric stresses. *Geophysical Journal International*, *226*(2), 1432–1460. https://doi.org/10.1093/gji/ggab108

Gradstein, F. M., Ogg, J. G., Schmitz, M. B., & Ogg, G. M. (Eds.). (2012). *The geologic time scale*. Elsevier.

Gurnis, M. (1988). Large-scale mantle convection and the aggregation and dispersal of supercontinents. *Nature*, *332*(6166), 695–699. https://doi.org/10.1038/332695a0

Gurnis, M. (1990). Bounds on global dynamic topography from Phanerozoic flooding of continental platforms. *Nature*, *344*(6268), 754–756. https://doi.org/10.1038/344754a0

Gurnis, M., Mitrovica, J. X., Ritsema, J., & van Heijst, H. J. (2000). Constraining mantle density structure using geological evidence of surface uplift rates: The case of the African Superplume. *Geochemistry, Geophysics, Geosystems*, *1*(7), e2020GC009025. https://doi.org/10.1029/1999GC000035

Gurnis, M., Turner, M., Zahirovic, S., DiCaprio, L., Spasojevic, S., Müller, R., et al. (2012). Plate tectonic reconstructions with continuously closing plates. *Computers & Geosciences*, *38*(1), 35–42. https://doi.org/10.1016/j.cageo.2011.04.014

Hager, B. H., Clayton, R. W., Richards, M. A., Comer, R. P., & Dziewonski, A. M. (1985). Lower mantle heterogeneity, dynamic topography and the geoid. *Nature*, *313*(6003), 541–545. https://doi.org/10.1038/313541a0

Hager, B. H., & Richards, M. A. (1989). Long-wavelength variations in Earth's geoid: Physical models and dynamical implications. *Philosophical Transactions of the Royal Society of London. Series A, Mathematical and Physical Sciences*, *328*(1599), 309–327. https://doi.org/10.1098/rsta.1989.0038

Hampson, G. J. (2010). Sediment dispersal and quantitative stratigraphic architecture across an ancient shelf. *Sedimentology*, *57*(1), 96–141. https://doi.org/10.1111/j.1365-3091.2009.01093.x

Hartley, R. A., Roberts, G. G., White, N., & Richardson, C. (2011). Transient convective uplift of an ancient buried landscape. *Nature Geoscience*, *4*(8), 562–565. https://doi.org/10.1038/ngeo1191

Hassan, R., Flament, N., Gurnis, M., Bower, D. J., & Müller, D. (2015). Provenance of plumes in global convection models. *Geochemistry, Geophysics, Geosystems*, *16*(5), 1465–1489. https://doi.org/10.1002/2015gc005751

Hayek, J. N., Vilacís, B., Bunge, H.-P., Friedrich, A. M., Carena, S., & Vibe, Y. (2020). Continent-scale Hiatus Maps for the Atlantic Realm and Australia since the Upper Jurassic and links to mantle flow induced dynamic topography. *Proceedings of the Royal Society A*, *476*, 2242. https://doi.org/10.1098/rspa.2020.0390

Hayek, J. N., Vilacís, B., Bunge, H.-P., Friedrich, A. M., Carena, S., & Vibe, Y. (2021). Correction: Continent-scale Hiatus Maps for the Atlantic Realm and Australia since the Upper Jurassic and links to mantle flow-induced dynamic topography. *Proceedings of the Royal Society A*, *477*, 2251. https://doi.org/10.1098/rspa.2021.0437

Hazzard, J. A., Richards, F. D., Goes, S. D., & Roberts, G. G. (2023). Probabilistic assessment of Antarctic thermomechanical structure: Impacts on ice sheet stability. *Journal of Geophysical Research: Solid Earth*, *128*(5), e2023JB026653. https://doi.org/10.1029/2023JB026653

Heine, C., Yeo, L. G., & Müller, R. D. (2015). Evaluating global paleoshoreline models for the Cretaceous and Cenozoic. *Australian Journal of Earth Sciences*, *62*(3), 275–287. https://doi.org/10.1080/08120099.2015.1018321

Hernández-Uribe, D., & Palin, R. M. (2019). Catastrophic shear-removal of subcontinental lithospheric mantle beneath the Colorado Plateau by the subducted Farallon slab. *Scientific Reports*, *9*(1), 8153. https://doi.org/10.1038/s41598-019-44628-y

Hintze, L., & Kowallis, B. (2009). *Geologic history of Utah, Brigham young University geology studies special publication 9*. Brigham Young University.

Hoggard, M. J., Austermann, J., Randel, C., & Stephenson, S. (2021). Observational estimates of dynamic topography through space and time. In H. Marquardt, M. Ballmer, S. Cottaar, & J. Konter (eds.) *Mantle convection and surface expressions*. https://doi.org/10.1002/9781119528609.ch15

Hoggard, M. J., Czarnota, K., Richards, F. D., Huston, D. L., Jaques, A. L., & Ghelichkhan, S. (2020). Global distribution of sediment-hosted metals controlled by craton edge stability. *Nature Geoscience*, *13*(7), 504–510. https://doi.org/10.1038/s41561-020-0593-2

Hoggard, M. J., White, N., & Al-Attar, D. (2016). Global dynamic topography observations reveal limited influence of large-scale mantle flow. *Nature Geoscience*, *9*(6), 456–463. https://doi.org/10.1038/10.1038/ngeo2709

Holdt, M. C., White, N. J., Stephenson, S. N., & Conway-Jones, B. W. (2022). Densely sampled global dynamic topographic observations and their significance. *Journal of Geophysical Research: Solid Earth*, *127*(7), e2022JB024391. https://doi.org/10.1029/2022JB024391

Hunter, W. C., & Smith, D. (1981). Garnet peridotite from Colorado Plateau ultramafic diatremes: Hydrates, carbonates, and comparative geothermometry. *Contributions to Mineralogy and Petrology*, *76*(3), 312–320. https://doi.org/10.1007/bf00375458

Huntington, K. W., Wernicke, B. P., & Eiler, J. M. (2010). Influence of climate change and uplift on Colorado Plateau paleotemperatures from carbonate clumped isotope thermometry. *Tectonics*, *29*(3), 1–19. https://doi.org/10.1029/2009TC002449

Jarvis, A., Reuter, H. I., Nelson, A., & Guevara, E. (2008). Hole-filled SRTM for the globe version 4, CGIAR-CSI SRTM 90 m database. Retrieved from http://srtm.csi.cgiar.org

Johnson, K. R., Nichols, D. J., & Hartman, J. H. (2002). Hell Creek formation: A 2001 synthesis. In J. H. Hartman, K. R. Johnson, & D. J. Nichols (Eds.), *The Hell Creek formation and the Cretaceous-Tertiary boundary in the Northern Great Plains: An integrated continental record of the end of the Cretaceous, Geological Society of America special paper 361, Boulder, CO* (pp. 503–510).

Katsura, T., Shatskiy, A., Manthilake, M. G. M., Zhai, S., Fukui, H., Yamazaki, D., et al. (2009). Thermal expansion of forsterite at high pressures determined by in situ X-ray diffraction: The adiabatic geotherm in the upper mantle. *Physics of the Earth and Planetary Interiors*, *174*(1–4), 86–92. https://doi.org/10.1016/j.pepi.2008.08.002

Klöcking, M., White, N. J., Maclennan, J., McKenzie, D., & Fitton, J. G. (2018). Quantitative Relationships Between Basalt Geochemistry, Shear Wave Velocity, and Asthenospheric Temperature Beneath Western North America. *Geochemistry, Geophysics, Geosystems*, *19*(9), 3376–3404. https://doi.org/10.1029/2018GC007559

Lamb, S., Moore, J. D., Perez-Gussinye, M., & Stern, T. (2020). Global whole lithosphere isostasy: Implications for surface elevations, structure, strength, and densities of the continental lithosphere. *Geochemistry, Geophysics, Geosystems*, *21*(10), e2020GC009150. https://doi.org/10.1029/2020GC009150

Laske, G., Masters, G., Ma, Z., & Pasyanos, M. (2013). Update on CRUST1.0—A 1-degree global model of Earth's crust. In *Geophysical research abstracts, 15, 2658, Vienna, Austria: EGU general assembly*.

Levandowski, W., Jones, C. H., Butcher, L. A., & Mahan, K. H. (2018). Lithospheric density models reveal evidence for Cenozoic uplift of the Colorado Plateau and Great Plains by lower-crustal hydration. *Geosphere*, *14*(3), 1–15. https://doi.org/10.1130/GES01619.1

Li, Z., & Aschoff, J. (2022). Constraining the effects of dynamic topography on the development of Late Cretaceous Cordilleran foreland basin, western United States. *GSA Bulletin*, *134*(1–2), 446–462. https://doi.org/10.1130/B35838.1

Lipp, A. G., & Roberts, G. G. (2021). Scale-dependent flow directions of rivers and the importance of subplate support. *Geophysical Research Letters*, *48*(1), e2020GL091107. https://doi.org/10.1029/2020GL091107

Liu, L., & Gurnis, M. (2008). Simultaneous inversion of mantle properties and initial conditions using an adjoint of mantle convection. *Journal of Geophysical Research*, *113*(B8), B08405. https://doi.org/10.1029/2008JB005594

Liu, L., Spasojević, S., & Gurnis, M. (2008). Reconstructing Farallon plate subduction beneath North America back to the Late Cretaceous. *Science*, *322*(January), 934–938. https://doi.org/10.5061/dryad.5t110

Liu, S., Nummedal, D., & Gurnis, M. (2014). Dynamic versus flexural controls of Late Cretaceous Western Interior Basin, USA. *Earth and Planetary Science Letters*, *389*, 221–229. https://doi.org/10.1016/j.epsl.2014.01.006

Lodhia, B. H., Roberts, G. G., Fraser, A. J., Fishwick, S., Goes, S., & Jarvis, J. (2018). Continental margin subsidence from shallow mantle convection: Example from West Africa. *Earth and Planetary Science Letters*, *481*, 350–361. https://doi.org/10.1016/j.epsl.2017.10.024

Lynds, R. M., & Slattery, J. S. (2017). Correlation of the upper Cretaceous strata of Wyoming, Wyoming State Geological Survey.

McKenzie, D., & Jarvis, G. (1980). The conversion of heat into mechanical work by mantle convection. *Journal of Geophysical Research*, *85*(B11), 6093–6096. https://doi.org/10.1029/JB085iB11p06093

McKenzie, D. P., Roberts, J. M., & Weiss, N. O. (1974). Convection in the Earth's mantle: Towards a numerical simulation. *Journal of Fluid Mechanics*, *62*(3), 465–538. https://doi.org/10.1017/S0022112074000784

Menard, H. W. (1969). Elevation and subsidence of oceanic crust. *Earth and Planetary Science Letters*, *6*(4), 275–284. https://doi.org/10.1016/0012-821X(69)90168-X

Merewether, E. A., Cobban, W. A., & Obradovich, J. D. (2011). Biostratigraphic data from upper Cretaceous formations–eastern Wyoming, central Colorado, and Northeastern New Mexico, U.S. Geological Survey Scientific investigations map 3175, 2 sheets, pamphlet (p. 10).

Merewether, E. A., & McKinney, K. C. (2015). *Composite biostratigraphic outcrop sections for Cretaceous formations along a south-trending transect from northwestern Montana to northwestern New Mexico* (Vol. 1258, p. 20151087). USGS.

Mitrovica, J. X., Beaumont, C., & Jarvis, G. T. (1989). Tilting of continental interiors by the dynamical effects of subduction. *Tectonics*, *8*(5), 1079–1094. https://doi.org/10.1029/TC008i005p01079

Mooney, W. D., & Kaban, M. K. (2010). The North American upper mantle: Density, composition, and evolution. *Journal of Geophysical Research*, *115*(B12), 2325. https://doi.org/10.1029/2010JB000866
Morris, M., Fernandes, V. M., & Roberts, G. G. (2020). Extricating dynamic topography from subsidence patterns: Examples from Eastern North America's passive margin. *Earth and Planetary Science Letters*, *530*, 115840. https://doi.org/10.1016/j.epsl.2019.115840
Moucha, R., Forte, A. M., Mitrovica, J. X., Rowley, D. B., Quéré, S., Simmons, N. A., & Grand, S. P. (2008). Dynamic topography and long-term sea-level variations: There is no such thing as a stable continental platform. *Earth and Planetary Science Letters*, *271*(1), 101–108. https://doi.org/10.1016/j.epsl.2008.03.056
Moucha, R., Forte, A. M., Rowley, D. B., Mitrovica, J. X., Simmons, N. A., & Grand, S. P. (2008). Mantle convection and the recent evolution of the Colorado Plateau and the Rio Grande Rift valley. *Geology*, *36*(6), 439–442. https://doi.org/10.1130/G24577A.1
Müller, R. D., Flament, N., Matthews, K. J., Williams, S. E., & Gurnis, M. (2016). Formation of Australian continental margin highlands driven by plate–mantle interaction. *Earth and Planetary Science Letters*, *441*, 60–70. https://doi.org/10.1016/j.epsl.2016.02.025
Müller, R. D., Hassan, R., Gurnis, M., Flament, N., & Williams, S. E. (2018). Dynamic topography of passive continental margins and their hinterlands since the Cretaceous. *Gondwana Research*, *53*, 225–251. https://doi.org/10.1016/j.gr.2017.04.028
Müller, R. D., Seton, M., Zahirovic, S., Williams, S. E., Matthews, K. J., Wright, N. M., et al. (2016). Ocean basin evolution and global-scale plate reorganization events since Pangea breakup. *Annual Review of Earth and Planetary Sciences*, *44*(1), 107–138. https://doi.org/10.1146/annurev-earth-060115-012211
Obradovich, J. D., & Cobban, W. A. (1975). A time-scale for the Late Cretaceous of the Western Interior of North America. *Geological Association of Canada Special Paper*, *13*, 31–54.
Panasyuk, S. V., & Hager, B. H. (2000). Inversion for mantle viscosity profiles constrained by dynamic topography and the geoid, and their estimated errors. *Geophysical Journal International*, *143*(3), 821–836. https://doi.org/10.1046/j.0956-540X.2000.01286.x
Pang, M., & Nummedal, D. (1995). Flexural subsidence and basement tectonics of the Cretaceous Western Interior basin, United States. *Geology*, *23*(2), 173–176. https://doi.org/10.1130/0091-7613(1995)023<0173:FSABTO>2.3.CO;2
Parsons, B., & Daly, S. (1983). The relationship between surface topography, gravity anomalies, and temperature structure of convection. *Journal of Geophysical Research*, *88*(B2), 1129–1144. https://doi.org/10.1029/JB088iB02p01129
Parsons, B., & Sclater, J. G. (1977). An analysis of the variation of ocean floor bathymetry and heat flow with age. *Journal of Geophysical Research*, *82*(5), 803–827. https://doi.org/10.1093/petrology/29.3.625
Pekeris, C. L. (1935). Thermal convection in the interior of the Earth. *Geophysical Journal International*, *3*, 343–367. https://doi.org/10.1111/j.1365-246X.1935.tb01742.x
Richards, F. D., Coulson, S. L., Hoggard, M. J., Austermann, J. A., Dyer, B., & Mitrovica, J. X. (2023). Geodynamically corrected Pliocene shoreline elevations in Australia consistent with midrange projections of Antarctic ice loss. *Science Advances*, *9*(46), eadg3035. https://doi.org/10.1126/sciadv.adg3035
Richards, F. D., Hoggard, M., Crosby, A., Ghelichkhan, S., & White, N. (2020). Structure and dynamics of the oceanic lithosphere-asthenosphere system. *Physics of the Earth and Planetary Interiors*, *309*, 106559. https://doi.org/10.1016/j.pepi.2020.106559
Richards, F. D., Hoggard, M. J., Cowton, L. R., & White, N. J. (2018). Reassessing the thermal structure of oceanic lithosphere with revised global inventories of basement depths and heat flow measurements. *Journal of Geophysical Research: Solid Earth*, *123*(10), 9136–9161. https://doi.org/10.1029/2018JB015998
Richards, F. D., Hoggard, M. J., White, N., & Ghelichkhan, S. (2020). Quantifying the relationship between short-wavelength dynamic topography and thermomechanical structure of the upper mantle using calibrated parameterization of anelasticity. *Journal of Geophysical Research: Solid Earth*, *125*(9), e2019JB019062. https://doi.org/10.1029/2019JB019062
Richards, M. A., & Hager, B. H. (1984). Geoid anomalies in a dynamic Earth. *Journal of Geophysical Research*, *89*(B7), 5987–6002. https://doi.org/10.1029/JB089iB07p05987
Riter, J. C. A., & Smith, D. (1996). Xenolith constraints on the thermal history of the mantle below the Colorado Plateau. *Geology*, *24*(3), 267–270. https://doi.org/10.1130/0091-7613(1996)024<0267:XCOTTH>2.3.CO;2
Roberts, G. G., Paul, J. D., White, N., & Winterbourne, J. (2012). Temporal and spatial evolution of dynamic support from river profiles: A framework for Madagascar. *Geochemistry, Geophysics, Geosystems*, *13*(4), 643. https://doi.org/10.1029/2012GC004040
Roberts, G. G., White, N. J., Martin-Brandis, G. L., & Crosby, A. G. (2012). An uplift history of the Colorado Plateau and its surroundings from inverse modeling of longitudinal river profiles. *Tectonics*, *31*(4), 1–25. https://doi.org/10.1029/2012TC003107.a
Roberts, L. N. R., & Kirschbaum, M. A. (1995). Paleogeography and the Late Cretaceous of the Western Interior of middle North America; coal distribution and sediment accumulation. In *USGS professional paper 1561*. https://doi.org/10.3133/pp1561
Rovere, A., Hearty, P. J., Austermann, J., Mitrovica, J. X., Gale, J., Moucha, R., et al. (2015). Mid-Pliocene shorelines of the US Atlantic Coastal Plain—An improved elevation database with comparison to Earth model predictions. *Earth-Science Reviews*, *145*, 117–131. https://doi.org/10.1016/j.earscirev.2015.02.007
Rowley, D. B., Forte, A. M., Moucha, R., Mitrovica, J. X., Simmons, N. A., & Grand, S. P. (2013). Dynamic topography change of the eastern United States since 3 million years ago. *Science*, *340*(6140), 1560–1563. https://doi.org/10.1126/science.1229180
Roy, M., Jordan, T. H., & Pederson, J. L. (2009). Colorado Plateau magmatism and uplift by warming of heterogeneous lithosphere. *Nature*, *459*(7249), 978–982. https://doi.org/10.1038/nature08052
Rudge, J. F., Champion, M. E. S., White, N., McKenzie, D., & Lovell, B. (2008). A plume model of transient diachronous uplift at the Earth's surface. *Earth and Planetary Science Letters*, *267*(1–2), 146–160. https://doi.org/10.1016/j.epsl.2007.11.040
Sahagian, D. (1988). Epeirogenic motions of Africa as inferred from Cretaceous shoreline deposits. *Tectonics*, *7*(1), 125–138. https://doi.org/10.1029/TC007i001p00125
Salles, T., Flament, N., & Müller, D. (2017). Influence of mantle flow on the drainage of eastern Australia since the Jurassic Period. *Geochemistry, Geophysics, Geosystems*, *18*(1), 280–305. https://doi.org/10.1002/2016GC006617
Schaeffer, A. J., & Lebedev, S. (2013). Global shear speed structure of the upper mantle and transition zone. *Geophysical Journal International*, *194*(1), 417–449. https://doi.org/10.1093/gji/ggt095
Schaeffer, A. J., & Lebedev, S. (2014). Imaging the North American continent using waveform inversion of global and USArray data. *Earth and Planetary Science Letters*, *402*, 26–41. https://doi.org/10.1016/j.epsl.2014.05.014
Schutt, D. L., & Lesher, C. E. (2006). Effects of melt depletion on the density and seismic velocity of garnet and spinel lherzolite. *Journal of Geophysical Research*, *111*(B5). https://doi.org/10.1029/2003JB002950
Sclater, J. G., & Christie, P. A. F. (1980). Continental stretching: An explanation for the post-Mid-Cretaceous subsidence of the Central North Sea Basin. *Journal of Geophysical Research*, *85*(B7), 3711–3739. https://doi.org/10.1029/JB085iB07p03711
Seton, M., Müller, R. D., Zahirovic, S., Gaina, C., Torsvik, T. H., Shephard, G., et al. (2012). Global continental and ocean basin reconstructions since 200 Ma. *Earth-Science Reviews*, *113*(3–4), 212–270. https://doi.org/10.1016/j.earscirev.2012.03.002

Shephard, G., Flament, N., Williams, S., Seton, M., Gurnis, M., & Müller, R. D. (2014). Circum-Arctic mantle structure and long-wavelength topography since the Jurassic. *Journal of Geophysical Research: Solid Earth*, *119*(10), 7889–7908. https://doi.org/10.1002/2014JB011078

Shephard, G., Müller, R. D., & Seton, M. (2013). The tectonic evolution of the Arctic since Pangea breakup: Integrating constraints from surface geology and geophysics with mantle structure. *Earth-Science Reviews*, *124*, 148–183. https://doi.org/10.1016/j.earscirev.2013.05.012

Smith, A. G., Smith, D. G., & Funnell, B. M. (1994). *Atlas of mesozic and cenozoic coastlines* (p. 99). Cambridge University Press.

Spasojević, S., & Gurnis, M. (2012). Sea level and vertical motion of continents from dynamic earth models since the Late Cretaceous. *AAPG Bulletin*, *96*(11), 2037–2064. https://doi.org/10.1306/03261211121

Stephenson, S. N., Hoggard, M., & White, N. (2021). Global continental residual topography. In *EGU general assembly conference abstracts* (p. EGU21-15505).

Stephenson, S. N., Roberts, G. G., Hoggard, M. J., & Whittaker, A. C. (2014). A Cenozoic uplift history of Mexico and its surroundings from longitudinal river profiles. *Geochemistry, Geophysics, Geosystems*, *15*(12), 4734–4758. https://doi.org/10.1002/2014GC005425

Stephenson, S. N., White, N. J., Li, T., & Robinson, L. F. (2019). Disentangling interglacial sea level and global dynamic topography: Analysis of Madagascar. *Earth and Planetary Science Letters*, *519*, 61–69. https://doi.org/10.1016/j.epsl.2019.04.029

Valentine, A. P., & Davies, D. R. (2020). Global Models From Sparse Data: A Robust Estimate of Earth's Residual Topography Spectrum. *Geochemistry, Geophysics, Geosystems*, *21*(8), e2020GC009240. https://doi.org/10.1029/2020GC009240

Van Der Meer, D. G., Spakman, W., Van Hinsbergen, D. J., Amaru, M. L., & Torsvik, T. H. (2010). Towards absolute plate motions constrained by lower-mantle slab remnants. *Nature Geoscience*, *3*(1), 36–40. https://doi.org/10.1038/ngeo708

Vilacìs, B., Hayek, J. N., Stotz, I. L., Bunge, H.-P., Friedrich, A. M., Carena, S., & Clark, S. (2022). Evidence for active upper mantle flow in the Atlantic and Indo-Australian realms since the Upper Jurassic from hiatus maps and spreading rate changes. *Proceedings of the Royal Society A*, *478*, 2262. https://doi.org/10.1098/rspa.2021.0764

Walker, J. D., Todd, D. B., Ross, A. B., Glazner, A., Farmer, L., & Richard, W. (2006). Navdat: A western North American volcanic and intrusive rock geochemical database. In *Special Paper of the Geological Society of America* (Vol. 397). https://doi.org/10.1130/2006.2397(05)

Wang, H., Gurnis, M., & Skogseid, J. (2020). Continent-wide drainage reorganization in North America driven by mantle flow. *Earth and Planetary Science Letters*, *530*, 115910. https://doi.org/10.1016/j.epsl.2019.115910

Watts, A. B. (2001). *Isostasy and flexure of the lithosphere*. Cambridge University Press.

Yamauchi, H., & Takei, Y. (2016). Polycrystal anelasticity at near-solidus temperatures. *Journal of Geophysical Research: Solid Earth*, *121*(11), 7790–7820. https://doi.org/10.1002/2016JB013316

Young, A., Flament, N., Williams, S. E., Merdith, A., Cao, X., & Müller, R. D. (2022). Long-term Phanerozoic sea level change from solid Earth processes. *Earth and Planetary Science Letters*, *584*, 117451. https://doi.org/10.1016/j.epsl.2022.117451

Ziegler, A., Rowley, D., Lottes, A., Sahagian, D., Hulver, M., & Gierlowski, T. (1985). Paleogeographic interpretation: With an example from the mid-Cretaceous. *Annual Review of Earth and Planetary Sciences*, *13*(1), 385–425. https://doi.org/10.1146/annurev.earth.13.1.385